

000 001 002 003 004 005 006 007 008 009 010 011 012 013 014 015 016 017 018 019 020 021 022 023 024 025 026 027 028 029 030 031 032 033 034 035 036 037 038 039 040 041 042 043 044 045 046 047 048 049 050 051 052 053 INFERENCE-TIME DYNAMIC MODALITY SELECTION FOR INCOMPLETE MULTIMODAL CLASSIFICATION

Anonymous authors

Paper under double-blind review

ABSTRACT

Multimodal deep learning (MDL) has achieved remarkable success across various domains, yet its practical deployment is often hindered by incomplete multimodal data. Existing incomplete MDL methods either discard missing modalities, risking the loss of valuable task-relevant information, or recover them, potentially introducing irrelevant noise, leading to the *discarding-imputation dilemma*. To address this dilemma, in this paper, we propose DyMo, a new inference-time dynamic modality selection framework that adaptively identifies and integrates reliable recovered modalities, fully exploring task-relevant information beyond the conventional discard-or-impute paradigm. Central to DyMo is a novel selection algorithm that maximizes multimodal task-relevant information for each test sample. Since direct estimation of such information at test time is intractable due to the unknown data distribution, we theoretically establish a connection between information and the task loss, which we compute at inference time as a tractable proxy. Building on this, a novel principled reward function is proposed to guide modality selection. In addition, we design a flexible multimodal network architecture compatible with arbitrary modality combinations, alongside a tailored training strategy for robust representation learning. Extensive experiments on diverse natural and medical datasets show that DyMo significantly outperforms state-of-the-art incomplete/dynamic MDL methods across various missing-data scenarios. Our code will be available at <https://github.com/anonymous>.

1 INTRODUCTION

Multimodal / multi-view deep learning (MDL), which integrates various modalities/views to achieve a multisensory perception akin to humans, has gained increasing attention and made significant advances in various domains such as healthcare (Acosta et al., 2022), marketing (Liu et al., 2024), and embodied intelligence (Duan et al., 2022). However, real-world deployment of these MDL models remains limited due to their simplified data assumptions. Existing MDL approaches typically presuppose full modality availability during inference. In practice, however, samples often lack one or more modalities due to heterogeneous collection protocols across centers, sensor malfunctions, or transmission errors (Wu et al., 2024a), leading to degraded model performance. Therefore, developing MDL models robust to incomplete multimodal data has become a critical research focus.

Current methods addressing missing modality can be broadly categorized into two types: (1) *recovery-based* approaches aim to impute missing modalities at the input level or in latent space via retrieval or generation, enabling the MDL model to operate as if all modalities were present (Ma et al., 2021; Xu et al., 2025); (2) *recovery-free* approaches are designed to ignore missing modalities and make predictions using only available ones (Lee et al., 2023; Wu et al., 2024b).

However, these incomplete MDL methods encounter intrinsic challenges in capturing task-relevant information under modality heterogeneity (Zhang et al., 2024). Specifically, modalities vary in their task relevance, due to differences in the strength of task-relevant signals and the degree of interfering, task-irrelevant noise (Huang et al., 2022b). As shown in Fig. 1(a), when highly informative modalities are missing, earlier recovery-free methods rely solely on the less distinguishable features of the remaining modalities, without considering the valuable task-relevant information contained in the missing ones, resulting in decreased model performance. Prior recovery-based methods appear to mitigate this issue by reconstructing missing modalities. Yet, imputation qualities often vary across

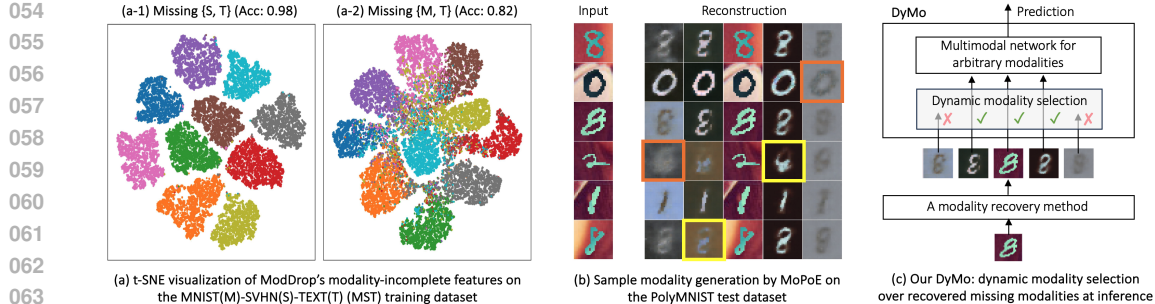


Figure 1: (a-b) Evidence of the *discarding-imputation dilemma*: (a-1) vs. (a-2) recovery-free methods (e.g., ModDrop (Neverova et al., 2015)) learn less discriminative features because they ignore highly task-relevant missing modalities $\{M, T\}$; (b) recovery-based methods (e.g., MoPoE (Sutter et al., 2021)) generate unreliable reconstructions, e.g., low-fidelity (orange) or misaligned (yellow) modalities. (c) Our DyMo, which addresses the dilemma by dynamically fusing task-relevant recovered modalities, improving accuracy by 5.67% on PolyMNIST and 1.68% on MST (Tab. 1).

samples due to cross-modal heterogeneity and diverse missing scenarios. As in Fig. 1(b), some recovered modalities may be *low-fidelity* (i.e., blurry or corrupted, orange boxes) or *semantically misaligned* (i.e., their labels are inconsistent with the input modalities, yellow boxes). Integrating such unreliable modalities can inject task-irrelevant noise, impairing decision-making. Thus, discarding missing modalities risks losing valuable task-relevant information, whereas restoring them may inject harmful information, a trade-off limitation we term the ***discarding-imputation dilemma***.

To address this dilemma in incomplete MDL, we introduce a new perspective that dynamically selects and fuses recovered modalities conditioned on their task relevance, moving beyond the conventional dichotomy of discarding vs. imputing missing data. A key technical challenge in such dynamic systems is how to estimate the task-relevant informativeness of each modality and identify unreliable modalities at inference time. Nevertheless, existing dynamic fusion approaches (Cao et al., 2024; Gao et al., 2024) are primarily designed for low-fidelity modalities and rely on modality-specific features for weighting, and thus are limited in identifying semantically misaligned modalities.

In this work, we propose DyMo, a novel inference-time dynamic modality selection framework that adaptively fuses reliable recovered modalities to maximize multimodal task-relevant information in incomplete MDL (see Fig. 1(c)). To avoid integrating unreliable (low-fidelity or misaligned) recovery, we propose a new dynamic algorithm that iteratively selects the most informative recovered modality based on the incremental multimodal task-relevant information gain it provides. Since the data distribution is unknown at inference, we theoretically derive that reducing task loss can increase the lower bound on task-relevant information. This motivates using the loss decrease as a practical proxy for information gain and introducing a novel principled reward function to guide modality selection. Additionally, to support flexible multimodal input, we design a multimodal network architecture capable of predicting task targets with arbitrary modalities. We further propose a tailored training strategy to learn robust latent features suitable for DyMo's dynamic selection process.

Our contributions can be summarized as follows. (1) To the best of our knowledge, we are the first to investigate the *discarding-imputation dilemma* in incomplete MDL and introduce dynamic neural networks to address it. (2) We propose DyMo, a novel dynamic framework that adaptively fuses recovered modalities via a new selection algorithm formulated on multimodal task-relevant information gain, together with a multimodal network and a tailored training algorithm for robust feature extraction from arbitrary combinations of modalities. (3) Experiments on 5 diverse datasets demonstrate DyMo's remarkable outperformance over incomplete/dynamic MDL SOTAs, especially under severe missing scenarios. DyMo is also easy-to-use (flexible with various modality recovery methods) and readily deployable without additional architecture overhead for its dynamic algorithm.

2 RELATED WORK

Incomplete Multimodal Deep Learning (MDL) methods (Zhan et al., 2025; Wu et al., 2024a) broadly fall into two categories: recovery-based and recovery-free. Recovery-based approaches can be further divided into offline and online, depending on when the imputation occurs. Offline methods

108 typically pre-train separate reconstruction networks, *e.g.*, variational auto-encoders (VAEs) (Sutter
 109 et al., 2021; Gao & Pu, 2025), and then use reconstructed data for downstream tasks. Online meth-
 110 ods (Wang et al., 2023b; Shou et al., 2025) jointly learn modality recovery and downstream tasks
 111 during training (Wang et al., 2023a). For instance, SMIL (Ma et al., 2022) employs Bayesian meta-
 112 learning to impute latent features, while M3Care (Zhang et al., 2022) retrieves similar samples to
 113 compensate for missing modalities. In recovery-free approaches, missing-agnostic techniques learn
 114 modality-invariant features via random modality dropout, *e.g.*, ModDrop (Neverova et al., 2015)
 115 and MMANet (Wei et al., 2023), or contrastive learning (Wu et al., 2024b), while missing-aware
 116 methods introduce missingness-specific parameters to handle different missing patterns (Ma et al.,
 117 2022; Li et al., 2025). However, previous incomplete MDL methods either fully recover or ignore
 118 missing modalities, without considering the *discarding-imputation dilemma*.

119 **Dynamic Deep Neural Networks**, in contrast to static models, can adapt their architectures and pa-
 120 rameters based on individual input, yielding substantial improvements in computational efficiency,
 121 accuracy, and interpretability (Han et al., 2021; Guo et al., 2024). Dynamic architecture methods
 122 adjust network depth, width, or routing paths on a per-sample basis (Fedus et al., 2022; Yue et al.,
 123 2024), while dynamic parameter algorithms modulate network weights or feature scaling without
 124 altering the architecture (Zhang et al., 2023). Our DyMo, which dynamically routes modality data
 125 conditioned on each instance, falls into the dynamic architecture category.

126 **Multimodal Fusion** is a critical research problem in MDL (Baltrušaitis et al., 2018). Existing meth-
 127 ods can be grouped by their fusion stage into early (data level), intermediate (feature level), and
 128 late (decision level) fusion. Recently, dynamic multimodal fusion methods have emerged to address
 129 instance-specific modality reliability variations. These methods assign different weights to each
 130 modality (Zhang et al., 2023; Gao et al., 2024) or selectively use a subset of modalities (Xue & Mar-
 131 culescu, 2023; Ma et al., 2025). However, such methods typically assume all modalities are available
 132 and mainly focus on intra-modality noise (*i.e.*, low-fidelity data) during training, lacking robustness
 133 against inter-modality errors (*i.e.*, semantic misalignment). While MICINet (Zhang et al., 2025)
 134 explores both types of noise, it requires ground-truth labels and cannot be applied during inference.
 135 By contrast, DyMo dynamically fuses observed and recovered modalities to handle incomplete data,
 136 while effectively addressing intra- and inter-modality noise without relying on labels.

3 METHOD

140 In this section, we present DyMo, a novel inference-time dynamic modality selection framework for
 141 incomplete multimodal classification by fully exploring task-relevant information from recovered
 142 modalities, while addressing the *discarding-imputation dilemma* (Fig. 1(c)). To achieve this, DyMo
 143 comprises 3 key components: (1) a flexible multimodal architecture capable of making predictions
 144 from arbitrary modalities (Sec. 3.1, Fig. 2); (2) a novel dynamic selection algorithm that integrates
 145 valuable recovered modalities to maximize multimodal task-relevant information for each sample
 146 (Sec. 3.2, Algorithm 1); and (3) a tailored training strategy that enhances representation learning to
 147 ensure feature robustness under dynamic modality configuration during inference (Sec. 3.3).

3.1 MULTIMODAL ARCHITECTURE FOR ARBITRARY MODALITIES

151 Our multimodal network is designed to produce reliable predictions from any subsets of input modal-
 152 ities, enabling adaptive fusion based on the task relevance of each recovered modality. To achieve
 153 this, we construct a multimodal network f (Fig. 2), consisting of modality-specific encoders for
 154 unimodal feature extraction, a multimodal transformer for modeling cross-modal interactions and
 155 learning a multimodal representation of available modalities, and a classifier for the final prediction.

156 A multimodal classification dataset can be defined as $\{\mathbb{X}_i, y_i\}_{i=1}^N$, where N is the number of sam-
 157 ples, $y_i \in \{1, \dots, K\}$ is the class label, and $\mathbb{X}_i = \{\mathbf{x}^{(m)}\}_{m \in \mathcal{I}_i}$ represents a (potentially incomplete)
 158 multimodal input comprising modalities such as images and text. Here, \mathcal{I}_i denotes a subset of the
 159 complete modality indices $[M] = \{1, 2, \dots, M\}$. Each available modality $m \in \mathcal{I}_i$ is encoded by a
 160 modality-specific encoder $h^{(m)}$, producing a sequence of feature tokens $\mathbf{H}^{(m)} \in \mathbb{R}^{L^{(m)} \times C}$, where
 161 $L^{(m)}$ is the sequence length. We then concatenate these tokens together with a learnable [CLS]
 token to form a multimodal sequence embedding. The [CLS] token’s output embedding serves as

162 the multimodal representation for classification as in (Devlin et al., 2019). To preserve the sequence
 163 structure across samples, we assign dummy tokens to the positions of missing modalities.
 164

165 Driven by transformer’s ability to capture long-range dependencies from variable lengths of
 166 the sequence, we build a multimodal transformer network ψ composed of T stacked trans-
 167 former layers (Vaswani et al., 2017) to learn cross-modal relations in observed modalities.
 168 These transformer layers conduct self-attention on the multi-
 169 modal sequence embedding and apply attention masks
 170 to ensure that missing modalities do not distort repres-
 171 entation learning. The extracted multimodal representation
 172 $z = \psi[h(\mathbb{X}_i)]$ from the transformer is passed through a lin-
 173 ear softmax classifier ζ to yield the final prediction.
 174

3.2 DYNAMIC MODALITY SELECTION AT INFERENCE

175 To address the *discarding-imputation dilemma*, we propose
 176 a novel dynamic modality selection algorithm that adap-
 177 tively discovers valuable task-relevant recovered modalities
 178 at inference. The core idea of our approach is a novel re-
 179 ward function that estimates the incremental multimodal
 180 task-relevant information contributed by each recovered
 181 modality. We establish a theoretical connection between
 182 information and task (*i.e.*, classification) loss, leading to an
 183 effective reward formulation linked to representation shift in
 184 the latent space. To further enhance
 185 robustness, we propose an intra-class similarity calibration for reward refinement based on training
 186 data. Finally, we introduce an iterative selection mechanism for reliable dynamic multimodal fusion.
 187

Multimodal Task-Relevant Information Reward (MTIR) is designed to estimate the incremental
 188 multimodal task-relevant information gained by adding a recovered modality to the existing ob-
 189 served modalities. MTIR is inspired by the notion of information gain (Ma et al., 2019; Jolliffe,
 190 2011) and aims to indicate the marginal impact of each recovered modality on the multimodal rep-
 191 resentation: (1) *Positive reward* suggests that the recovered modality introduces additional task-
 192 relevant information that enhances the representation; (2) *Zero reward* indicates that the recovery is
 193 of low fidelity, mainly introducing noise and providing negligible benefit; and (3) *Negative reward*
 194 implies that the recovery contains task-relevant but semantically inconsistent information, poten-
 195 tially degrading the representation. This formulation enables the identification of both low-fidelity
 196 and misaligned modalities, which have been largely overlooked in prior dynamic MDL work.
 197

To quantify task-relevant information contained in the multimodal representation, we consider mu-
 198 tual information between the multimodal representations \mathbf{Z} and the target labels Y :
 199

$$I(Y; \mathbf{Z}) = \mathbb{E}_{p(y, \mathbf{z})} \log \frac{p(y, \mathbf{z})}{p(y)p(\mathbf{z})}. \quad (1)$$

200 Since the true data distributions are unknown at inference, we propose to derive a lower bound of
 201 $I(Y; \mathbf{Z})$, estimated using the empirical **test** classification cross-entropy (CE) loss $\hat{\mathcal{L}}_{\text{ce}}$:
 202

$$I(Y; \mathbf{Z}) \geq H(Y) - \hat{\mathcal{L}}_{\text{ce}} - G \sqrt{\frac{\ln(1/\delta)}{2|\mathcal{D}|}}, \quad \text{with probability at least } 1 - \delta, \quad (2)$$

203 where $H(Y)$ is the entropy of the target labels, G is a conservative upper bound on the per-sample
 204 CE loss, $|\mathcal{D}|$ is the size of a test dataset, and $\delta \in (0, 1)$ controls the probability of the bound holding
 205 (detailed derivation in Appendix A.1). This bound formalizes the intuition that reducing $\hat{\mathcal{L}}_{\text{ce}}$ can
 206 increase the lower bound on $I(Y; \mathbf{Z})$, thereby potentially increasing the task-relevant information
 207 in \mathbf{Z} . Motivated by this insight, we propose to use the empirical **test** CE loss decrease as a tractable
 208 proxy for information gain, forming the theoretical foundation of our MTIR reward.
 209

210 Given an incomplete multimodal test sample $\mathbb{X}_j = \{\mathbf{x}^{(m)}\}_{m \in \mathcal{I}_j}$, we recover the missing modalities
 211 as $\tilde{\mathbb{X}}_j = \{\tilde{\mathbf{x}}^{(u)}\}_{u \in ([M] \setminus \mathcal{I}_j)}$ using a recovery function Υ (*e.g.*, a VAE). The empirical CE loss of
 212 DyMo g , including a multimodal network f and a dynamic selection algorithm, is then defined as:
 213

$$\hat{\mathcal{L}}_{\text{ce}} = \frac{1}{|\mathcal{D}|} \sum_{j=1}^{|\mathcal{D}|} \ell_{\text{ce}} \left[g_j(\mathbb{X}_j, \tilde{\mathbb{X}}_j), y_j \right]. \quad (3)$$

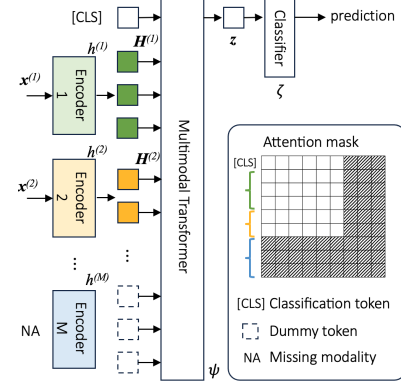


Figure 2: Multimodal network architec-
 ture f for arbitrary modalities.

in the latent space. To further enhance
 robustness, we propose an intra-class similarity calibration for reward refinement based on training
 data. Finally, we introduce an iterative selection mechanism for reliable dynamic multimodal fusion.

To minimize $\hat{\mathcal{L}}_{ce}$, DyMo should adaptively integrate the recovered modalities in $\tilde{\mathbb{X}}$ that reduce per-sample loss ℓ_{ce} . Accordingly, for each sample, we define MTIR of u -th recovered modality as:

$$R(\tilde{\mathbf{x}}^{(u)}, \mathbb{X}^O) = \ell_{ce}[f(\mathbb{X}^O), y] - \ell_{ce}[f(\mathbb{X}^O, \tilde{\mathbf{x}}^{(u)}), y] = -\log p_f(y|\mathbf{z}) + \log p_f(y|\mathbf{z}^u), \quad (4)$$

where \mathbb{X}^O denotes the observed modalities (initially \mathbb{X}), $\ell_{ce} = -\log p_f(y|\mathbf{z})$, $\mathbf{z} = \psi[h(\mathbb{X}^O)]$, and $\mathbf{z}^u = \psi[h(\mathbb{X}^O, \tilde{\mathbf{x}}^{(u)})]$. Since the true label y is unknown at inference, we substitute it with the predicted labels $\hat{y} = \text{argmax } f(\mathbb{X}^O)$ and $\hat{y}^u = \text{argmax } f(\mathbb{X}^O, \tilde{\mathbf{x}}^{(u)})$. However, such substitution may undermine the reliability of MTIR, especially under mispredictions or overfitting. To mitigate this, inspired by the robustness and generalizability of metric learning (Vinyals et al., 2016; Chen et al., 2020), we further investigate the representation shifts with respect to the training distribution, measured in the latent space. Specifically, we treat classification as a mixture density estimation problem in feature space, where each class corresponds to a component. Suppose equal class prior probability and exponential family distributions, the posterior probability of $y = k$ given \mathbf{z} is:

$$p(y = k|\mathbf{z}) = \frac{\exp(-d_\phi(\mathbf{z}, \mathbf{c}_k))}{\sum_{k'=1}^K \exp(-d_\phi(\mathbf{z}, \mathbf{c}_{k'}))}, \quad \mathbf{c}_k = \frac{1}{\sum_{i=1}^N \mathbb{I}[y_i = k]} \sum_{i:y_i=k} \mathbf{z}_i, \quad (5)$$

where d_ϕ is a Bregman-divergence type distance function (Banerjee et al., 2005) (e.g., squared Euclidean distance), and \mathbf{c}_k is the class prototype estimated from the training dataset. The derivation of this expression is provided in Appendix A.2. Substituting Eq. 5 into Eq. 4 yields:

$$R(\tilde{\mathbf{x}}^{(u)}, \mathbb{X}^O) = -\log \frac{\exp(-d_\phi(\mathbf{z}, \mathbf{c}_{\hat{y}}))}{\sum_{k'=1}^K \exp(-d_\phi(\mathbf{z}, \mathbf{c}_{k'}))} + \log \frac{\exp(-d_\phi(\mathbf{z}^u, \mathbf{c}_{\hat{y}^u}))}{\sum_{k'=1}^K \exp(-d_\phi(\mathbf{z}^u, \mathbf{c}_{k'}))}. \quad (6)$$

This formula indicates that higher MTIR rewards can be obtained when the representation moves closer to the class prototype after incorporating a recovered modality, which is consistent with the intuition that fusing effective information increases the model’s predictive certainty (Dai et al., 2023).

Intra-Class Similarity Calibration: Eq. 6 defines the MTIR reward based on changes in the distance between a sample representation and its predicted class prototype. A challenging case arises when \hat{y} and \hat{y}^u differ, while \mathbf{z} and \mathbf{z}^u lie at similar distances from their respective prototypes, yielding a near-zero reward. To address this and enhance the reliability of the MTIR reward, we introduce a novel calibration term α , which refines the reward by accounting for how representative a sample is within its predicted class cluster. The calibrated MTIR reward R^* is:

$$R^*(\tilde{\mathbf{x}}^{(u)}, \mathbb{X}^O) = -\log \frac{\exp(-d_\phi(\mathbf{z}, \mathbf{c}_{\hat{y}}))}{\sum_{k'=1}^K \exp(-d_\phi(\mathbf{z}, \mathbf{c}_{k'}))} + \alpha \times \log \frac{\exp(-d_\phi(\mathbf{z}^u, \mathbf{c}_{\hat{y}^u}))}{\sum_{k'=1}^K \exp(-d_\phi(\mathbf{z}^u, \mathbf{c}_{k'}))}. \quad (7)$$

To compute α , we first define the intra-class similarity (ICS) score of \mathbf{z} for class k . Instead of computing distances to all training samples in class k , we propose an efficient approximation. Specifically, we approximate the distribution of distances from the samples in class k to the class prototype \mathbf{c}_k as a truncated normal distribution $d_\phi \sim \mathcal{N}(0, \sigma_k)$, $d_\phi > 0$, where σ_k is estimated from the training data. The ICS score is then written as:

$$ICS(y = k, \mathbf{z}) = \mathbb{P}(d_\phi > d_\phi(\mathbf{z}, \mathbf{c}_k) | d_\phi > 0) = 2(1 - \Phi(d_\phi(\mathbf{z}, \mathbf{c}_k))), \quad (8)$$

where Φ is the cumulative distribution function of the normal distribution. ICS quantifies the representativeness of \mathbf{z} within a class cluster, with a higher value indicating closer alignment with the training samples in that cluster.

The calibration term is defined as the ratio between the ICS scores of \mathbf{z}^u and \mathbf{z} : $\frac{ICS(y = \hat{y}^u, \mathbf{z}^u)}{ICS(y = \hat{y}, \mathbf{z})}$. Since \mathbb{X}^O are observed, task-relevant modalities, while $\tilde{\mathbf{x}}^{(u)}$ is synthetic and can introduce unreliable information, DyMo should be conservative when $ICS(y = \hat{y}^u, \mathbf{z}^u) > ICS(y = \hat{y}, \mathbf{z})$. To this end, we introduce an asymmetric α :

$$\alpha = \begin{cases} 1 & \text{if } ICS(y = \hat{y}^u, \mathbf{z}^u) > ICS(y = \hat{y}, \mathbf{z}), \\ \frac{ICS(y = \hat{y}^u, \mathbf{z}^u)}{ICS(y = \hat{y}, \mathbf{z})} & \text{otherwise,} \end{cases} \quad (9)$$

which is used to calculate R^* in Eq. 7. Thus, if \mathbf{z}^u is less representative than \mathbf{z} within its predicted class cluster (i.e., $\alpha < 1$), the second term in R is down-weighted, reducing the calibrated MTIR.

Iterative Modality Selection: To improve the reliability of DyMo’s dynamic process, we introduce an iterative selection algorithm to maximize multimodal task-relevant information for each sample (Algorithm 1). At each step, given an observed set \mathbb{X}^O and a candidate set \mathbb{X}^C , we add the recovered modality with the highest MTIR reward to \mathbb{X}^O while removing all ineffective modalities with non-positive rewards from \mathbb{X}^C . This stepwise selection ensures that DyMo incorporates only the most informative modalities, effectively mitigating noise accumulation.

Algorithm 1: DyMo Adaptive Inference

Input: Test dataset \mathcal{D} , network f (including h , ψ , and ζ), and a recovery method Υ

for each test sample $\bar{\mathbb{X}} = \{\bar{x}^{(m)}\}_{m \in \mathcal{I}} \in \mathcal{D}$ **do**

$\hat{\mathbb{X}} = \{\hat{x}^{(u)}\}_{u \in [M] \setminus \mathcal{I}} \leftarrow \Upsilon(\bar{\mathbb{X}})$; // Recover missing modalities

$\mathbb{X}^O \leftarrow \bar{\mathbb{X}}, \quad \mathbb{X}^C \leftarrow \hat{\mathbb{X}}$; // Initialize observed & candidate modality sets

while $\mathbb{X}^C \neq \emptyset$ **do**

$r^{*(i)} \leftarrow R^*(\bar{x}^{(i)}, \mathbb{X}^O), \quad \forall \bar{x}^{(i)} \in \mathbb{X}^C$; // Calibrated MTIR reward (Eq. 7)

$k \leftarrow \arg \max_i r^{*(i)}$; // Best candidate modality index

if $r^{*(k)} > 0$ **then**

$\mathbb{X}^O \leftarrow \mathbb{X}^O \cup \bar{x}^{(k)}$; // Integrate the most informative modality

end

$\mathbb{X}^C \leftarrow \mathbb{X}^C \setminus \{\bar{x}^{(i)} \mid r^{*(i)} \leq 0\}$; // Remove ineffective modalities

end

$\hat{y} \leftarrow f(\mathbb{X}^O)$

end

return All test predictions $\hat{\mathcal{Y}}$ collected over \mathcal{D}

3.3 TRAINING ALGORITHM

DyMo's dynamic inference relies on representation shifts, making it essential to train our multimodal network f properly to learn a robust latent feature space where samples of the same class cluster together despite missing modalities. To achieve this, we design incomplete-modality simulation training and an auxiliary missing-agnostic contrastive loss.

Incomplete Simulation Training. To guarantee that f extracts robust task-relevant features across various missing patterns, we propose a simple yet effective random sampling strategy during training. In specific, each complete multimodal sample $\{\mathbf{x}^{(1)}, \dots, \mathbf{x}^{(M)}\}$ has $2^M - 1$ non-empty modality subsets. In each minibatch, we randomly sample A such subsets for classification loss calculation:

$$\mathcal{L}_{\text{class}} = -\frac{1}{A} \frac{1}{B} \sum_{\mathcal{S} \sim \mathcal{U}_A} \sum_{i=1}^B \log p_f \left(y_i \mid \{\boldsymbol{x}^{(m)}\}_{m \in \mathcal{S}} \right), \quad (10)$$

where B is the batch size, and $\mathcal{U}_A \sim \text{Uniform}_{\text{w/o rep}}(\mathcal{P}([M]) \setminus \emptyset, A)$. $\mathcal{P}([M])$ denotes a collection of all modality subsets. This strategy reduces computational cost compared to prior work (Ma et al., 2022) that requires all missing patterns in each training step.

Auxiliary Missing-Agnostic Contrastive Loss is designed to further enhance intra-class clustering and inter-class separation regardless of missing scenarios:

$$\mathcal{L}_{\text{aux}} = -\frac{1}{A} \frac{1}{B} \sum_{\mathcal{S} \sim \mathcal{U}_A} \sum_{i=1}^B \log \frac{\exp(-d_{\phi}(\mathbf{z}_i, \mathbf{c}_{y_i})/t)}{\sum_{k'=1}^K \exp(-d_{\phi}(\mathbf{z}_i, \mathbf{c}_{k'})/t)}, \quad (11)$$

where t is the temperature parameter. In experiments, we test two common distance functions: the squared Euclidean distance $d_\phi(\mathbf{u}, \mathbf{v}) = \|\mathbf{u} - \mathbf{v}\|_2^2$ and the cosine distance $d_\phi(\mathbf{u}, \mathbf{v}) = 1 - (\mathbf{u} \cdot \mathbf{v}) / (\|\mathbf{u}\|_2 \|\mathbf{v}\|_2)$, where $\mathbf{u} \cdot \mathbf{v}$ is the dot product of the vectors.

Overall Loss. The final training loss for DyMo is expressed as $\mathcal{L}_{\text{overall}} = \mathcal{L}_{\text{class}} + \mathcal{L}_{\text{aux}}$.

4 EXPERIMENT

Datasets and Evaluation Metrics: We conduct extensive experiments on 5 different datasets with varied modalities, including 3 simulated benchmark datasets (Sutter et al., 2021): PolyMNIST, MST, and biomodal CelebA, and two large real-world datasets: a natural image dataset, Data Visual Marketing (DVM) (Huang et al., 2022a), and a medical image dataset, UK Biobank (UKBB) (Sudlow et al., 2015). For UKBB, we focus on two cardiac disease classification tasks: coronary artery disease (CAD) and myocardial infarction, using magnetic resonance (MR) images and disease-related tabular features. Following (Du et al., 2025; Sutter et al., 2020), we report the area under the curve (AUC) for UKBB, and accuracy for the remaining datasets. Dataset details are in Appendix B.1.

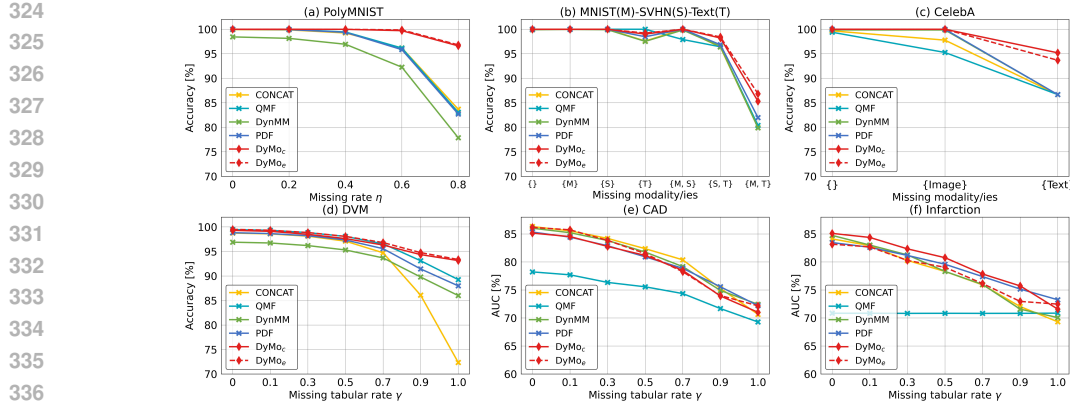


Figure 3: Comparison of DyMo with static/dynamic multimodal fusion techniques on 6 multimodal classification tasks under various missing scenarios. DyMo_c and DyMo_e denote the use of cosine and squared Euclidean distances, respectively.

Implementation Details: For the recovery method in DyMo, we leveraged MoPoE (Sutter et al., 2021), a multimodal VAE network, for PolyMNIST, MST, and CelebA. Then, for DVM and UKBB, we used TIP (Du et al., 2024), an image-tabular reconstruction framework. Note that DyMo can be deployed with any recovery method. To ensure a fair comparison, all compared methods used the same modality-specific encoders as DyMo. Models were trained on complete datasets and evaluated under various missing scenarios: (i) For PolyMNIST, we set 5 missing rates $\eta = \{0, 0.2, 0.4, 0.6, 0.8\}$, where each sample randomly misses $\eta \times 100\%$ modalities; (ii) For MST and CelebA, we tested different combinations of missing modalities; (iii) For DVM and UKBB, since TIP is a table reconstruction network, we evaluated both full- and intra-table (*i.e.*, partial within-modality) missing. Specifically, we set 7 missing tabular rates $\gamma = \{0, 0.1, 0.3, 0.5, 0.7, 0.9, 1\}$, where each sample randomly misses $\gamma \times 100\%$ tabular features. Note that DyMo can also handle incomplete modality training, as our multimodal network supports arbitrary modalities. Detailed implementation settings for all models are provided in Appendix B.2.

4.1 OVERALL RESULTS

Comparing Against Multimodal Static / Dynamic Fusion SOTAs: To assess DyMo’s effectiveness in selecting valuable task-relevant recovered modalities at inference, we compared it with SOTA multimodal fusion techniques, including static concatenation-based fusion (**CONCAT**) (Baltrušaitis et al., 2018) and 3 dynamic fusion methods, **QMF** (Zhang et al., 2023), **DynMM** (Xue & Marculescu, 2023), and **PDF** (Cao et al., 2024). All methods were provided with the same set of non-missing and recovered modalities at inference. Notably, prior dynamic methods typically require **additional modality-specific branches for modality contribution estimation** or multi-stage training, whereas DyMo operates directly on multimodal representations **without extra modality-specific parameters and relies on single-stage training**. We report DyMo’s results using cosine distance (DyMo_c) and squared Euclidean distance (DyMo_e).

As shown in Fig. 3, DyMo achieves substantial improvements on most datasets, especially under severe missing scenarios. For example, DyMo achieves 13.12% higher accuracy on PolyMNIST with 80% missing modalities and 4.11% higher accuracy on DVM when the full table is missing. Both DyMo_c and DyMo_e **consistently outperform prior SOTAs on most datasets**, demonstrating DyMo’s robustness to the choice of distance metric. We further observe that (1) performance decreases vary across different missing modality combinations (Fig. 3(b,c)), indicating the existence of varying modality task relevance; (2) prior dynamic methods outperform static fusion on DVM (Fig. 3(d)) but achieve limited gains on the 3 simulated benchmarks (Fig. 3(a-c)). This limitation arises because VAE-based reconstruction tends to produce visually plausible but class-misaligned recovered modalities, which prior dynamic methods struggle to handle. By contrast, DyMo addresses this via estimating incremental multimodal task-relevant information gain, resulting in superior results. Additionally, DyMo and CONCAT perform similarly on CAD, likely due to the consistent informa-

378 Table 1: Comparison of DyMo with recovery-based and recovery-free incomplete MDL methods
 379 on 6 multimodal classification tasks under various missing scenarios. Models marked with \dagger were
 380 trained using our proposed incomplete modality simulation. Complete results for all missing scenarios
 381 are provided in Appendix C.1.

Model	PolyMNIST Acc (%) \uparrow			MST Acc (%) \uparrow			CelebA Acc (%) \uparrow			DVM Acc (%) \uparrow			CAD AUC (%) \uparrow			Infarction AUC (%) \uparrow		
	Missing Rate η			Missing Modality/ies			Missing Modality/ies			Missing Tabular Rate γ			Missing Tabular Rate γ			Missing Tabular Rate γ		
	0	0.6	0.8	{}	{S,T}	{M,T}	{}	{I}	{T}	0	0.7	1	0	0.7	1	0	0.7	1
(a) Recovery-based Methods for Missing Modality																		
MultiAE	99.77	95.36	84.39	99.96	97.00	81.60	89.98	15.51	89.71	-	-	-	-	-	-	-	-	-
MultiAE \dagger	99.94	97.50	89.86	99.87	98.33	83.44	88.66	72.04	87.44	-	-	-	-	-	-	-	-	-
MoPoE	99.79	93.93	79.84	99.62	90.86	79.01	38.97	13.91	34.84	-	-	-	-	-	-	-	-	-
MoPoE \dagger	99.63	96.81	87.06	99.39	96.50	82.54	68.22	56.90	65.75	-	-	-	-	-	-	-	-	-
M3Care	99.93	56.66	40.53	99.99	16.03	9.34	92.33	99.92	51.75	98.44	-	11.92	85.62	-	64.99	70.61	-	70.53
M3Care \dagger	99.99	97.27	87.92	99.98	98.27	85.16	98.73	97.14	91.32	98.94	-	93.43	72.48	-	72.48	83.27	-	68.44
OnlineMAE	100	98.29	90.09	99.90	98.14	86.14	86.67	86.67	90.92	-	89.90	85.22	-	70.96	84.05	-	61.39	
(b) Recovery-free Methods for Missing Modality																		
ModDrop	99.97	97.66	88.44	100	98.21	82.47	99.93	99.93	87.32	99.02	93.23	87.97	85.10	76.65	69.18	84.76	74.64	72.16
MTL	99.97	98.43	91.14	99.96	98.60	84.37	99.69	99.26	89.38	99.44	95.53	92.32	84.87	77.72	70.23	83.59	75.73	69.90
MAP	99.86	43.00	23.19	100	9.83	10.13	99.98	99.93	85.33	98.86	86.96	63.15	84.39	75.61	70.11	84.62	71.73	69.17
MAP \dagger	99.99	96.74	76.20	99.99	97.84	11.36	100	99.99	86.06	99.37	94.83	91.15	85.26	75.84	68.76	85.49	75.88	70.81
MUSE	99.93	94.73	77.56	99.86	97.14	35.96	99.93	99.86	88.35	96.86	-	1.64	83.47	-	53.23	84.40	-	66.78
(c) Dynamic Recovery Method for Missing Modality																		
DyMo _c	100	99.71	96.61	100	98.22	85.31	100	100	95.20	99.30	96.31	93.14	85.14	78.49	71.02	85.10	77.85	71.58
DyMo _e	100	99.87	96.81	100	98.43	86.84	100	100	93.67	99.50	96.81	93.36	86.17	78.24	72.17	83.16	76.14	72.47

396 Table 2: Ablation study of DyMo. Baseline integrates all recovered modalities without selection. S
 397 integrates all modalities with positive reward ($r > 0$) simultaneously. I iteratively adds the modality
 398 with the highest r . C uses the calibrated reward r^* , obtained via intra-class similarity calibration.

Dynamic selection	C	PolyMNIST		MST		CelebA		DVM		CAD		Infarction	
		0.6	0.8	{S,T}	{M,T}	{I}	{T}	0.7	1	0.7	1	0.7	1
Baseline		96.80	84.21	96.43	80.73	100	86.67	96.27	88.36	79.15	71.84	78.31	74.89
S		99.59	94.33	97.21	82.08	100	86.67	96.54	92.83	79.44	72.20	77.83	75.27
I		99.60	94.50	97.26	82.12	100	86.67	96.54	92.83	79.44	72.20	77.83	75.27
I	\checkmark	99.71	96.61	98.22	85.31	100	95.20	96.31	93.14	78.49	71.02	77.85	71.58

404 tiveness of the recovered table modality across samples, leaving limited room for dynamic fusion to
 405 further improve performance.

406 **Comparing Against Incomplete MDL SOTAs:** To evaluate DyMo’s efficacy in handling missing
 407 modalities, we compared it with SOTA incomplete MDL approaches, including 4 recovery-based
 408 (**MultiAE** (Ngiam et al., 2011), **MoPoE** (Sutter et al., 2021), **M3Care** (Zhang et al., 2022), and
 409 **OnlineMAE** (Woo et al., 2023)) and 4 recovery-free methods (**ModDrop** (Neverova et al., 2015),
 410 **MTL** (Ma et al., 2022), **MAP** (Lee et al., 2023), and **MUSE** (Wu et al., 2024b)). For models without
 411 simulating different missing scenarios during training, we additionally report their results with our
 412 incomplete simulation training. Since ModDrop is a training scheme rather than a standalone archi-
 413 tecture, we applied it to the same multimodal backbone as DyMo for a fair comparison. Methods
 414 requiring task-specific decoders or restricted to full-modality missing settings were evaluated only
 415 on datasets where such decoders are provided and under full-modality missingness.

416 In Tab. 1, integrating our incomplete simulation training improves model performance (w/ vs. w/o
 417 \dagger), demonstrating its effectiveness in learning features robust to missing data. We also observe
 418 the *discarding-imputation dilemma*: (i) recovery-free methods suffer large performance drops when
 419 highly task-relevant modalities are missing, e.g., a 61.18% accuracy reduction for MUSE on MST
 420 with missing {M,T} vs. {S,T}; (ii) recovery-based methods struggle under severe missing scenarios,
 421 e.g., OnlineMAE’s accuracy on PolyMNIST decreases by 9.91% with $\eta = 0.8$ vs. $\eta = 0$, indicating
 422 the generation of unreliable recoveries. In contrast, DyMo effectively addresses this dilemma,
 423 significantly outperforming prior SOTAs on full- and intra-modality missing conditions, e.g., 5.67%
 424 higher accuracy on PolyMNIST with 80% missing modalities and 1.97% higher AUC on Infarction
 425 with 70% missing tabular features. Performance matches M3Care \dagger on DVM and CAD when $\eta = 1$,
 426 likely due to TIP’s limited full-table reconstruction; stronger recovery could further enhance results.

427 4.2 ABLATION STUDY AND VISUALIZATION

428 **Effectiveness of Key Model Components:** We ablated the key components of DyMo in Tab. 2,
 429 including the MTIR reward, iterative selection, and the calibration term. The results show that in-
 430 tegrating all recovered modalities without selection can introduce task-irrelevant information and

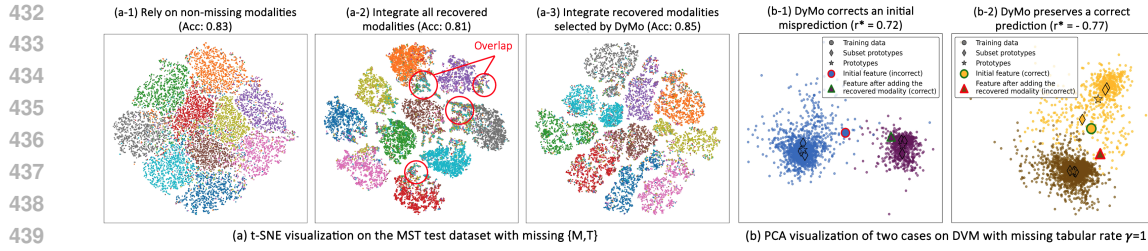


Figure 4: (a) t-SNE visualization of DyMo_c on MST with different modality inputs: (a-1) using only non-missing modalities; (a-2) integrating all recovered modalities without selection; (a-3) incorporating recovered modalities selected by DyMo_c. (b) PCA visualizations of two successful DyMo_c’s test cases on DVM: (b-1) a misprediction corrected by incorporating a recovered modality; (b-2) a correct prediction maintained by disregarding an unreliable recovered modality.

degrade performance. Each component contributes positively, and DyMo, which combines all of them, achieves the best overall results. For CAD and Infarction, I outperforms $I+C$. This is likely because the calibration term, bounded between 0 and 1, makes the model more conservative in modality selection. In these cases, the recovered table consistently provides task-relevant information, so omitting C allows more samples to benefit from it. Tuning a dataset-specific scaling hyper-parameter before applying C may mitigate this issue, which we leave for future work. Additional ablation studies on our incomplete simulation training, generalizability analysis of DyMo, and adaptive inference analysis can be found in Appendix C.2-C.3.

Visualization of Multimodal Representations and Case Studies: To examine the effect of integrating recovered modalities selected by DyMo in shaping the latent space, we used t-SNE (Maaten & Hinton, 2008) to visualize the multimodal embeddings of the test set. Fig. 4(a) shows that integrating all recovered modalities increases inter-class separation; however, samples with unreliable recoveries can be embedded within incorrect class clusters, leading to misclassifications and degraded performance. In contrast, DyMo’s dynamic fusion alleviates this issue, producing a more discriminative latent space and improved classification results. Moreover, we conducted case studies at both the feature level (PCA (Jolliffe, 2011) visualization, Fig. 4(b)) and the input level (Fig. 5(b)), illustrating that DyMo effectively selects reliable, task-relevant recovered modalities that enhance model performance. A challenging example is shown in the fourth row of Fig. 5(b), where all dynamic methods struggle due to noisy observed modalities and semantically misaligned recovered modalities. Additional visualizations and detailed analyses are provided in Appendix C.5.

Prediction Transition: We analyzed prediction changes before and after dynamic modality selection using a Sankey diagram. In Fig. 5(a), DyMo corrects many initial mispredictions and achieves improved performance, highlighting the benefit of recovered modalities. A small fraction of correct predictions become incorrect after updating, likely due to limited recovery quality, suggesting that stronger recovery methods could reduce such errors. Reconstruction analyses of modality recovery methods are in Appendix C.6.

5 CONCLUSION

In conclusion, we present the first study on dynamic multimodal fusion after modality recovery for addressing missing modalities. We propose DyMo, a new inference-time dynamic modality selection framework that fully explores task-relevant information while addressing the *discarding-imputation dilemma* by adaptively identifying and fusing valuable recovered modalities. DyMo introduces a novel selection algorithm grounded in maximizing multimodal task-relevant informa-

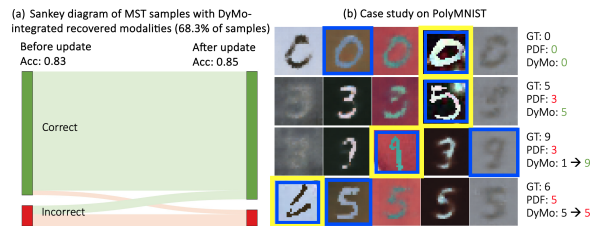


Figure 5: (a) Sankey diagram for DyMo_c prediction transitions on MST with missing {M,T}. (b) Case study on PolyMNIST, where yellow indicates non-missing modalities, while blue indicates modalities selected by DyMo_c.

486
487
488
489
490
491
492
493
494
495
496
497
498
499
500
501
502
503
504
505
506
507
508
509
510
511
512
513
514
515
516
517
518
519
520
521
522
523
524
525
526
527
528
529
530
531
532
533
534
535
536
537
538
539
tion and proposes a principled reward function. We further design a flexible multimodal network architecture and a tailored training strategy to enable robust multimodal representation learning under arbitrary modality combinations. Experiments on various natural and medical datasets showed DyMo’s SOTA performance and the efficacy of its components. With the growing demand for multimodal deep learning, DyMo offers significant potential for real-world deployment on incomplete data. Future work will explore extensions to other tasks (*e.g.*, segmentation) and modalities (*e.g.*, video). We note that large language models (LLMs) were used solely to improve language clarity; all scientific content and ideas were developed by the authors.

540 **Ethics Statement:** This research complies with the ICLR Code of Ethics. The study makes use
 541 of multiple datasets: publicly available benchmarks and the UK Biobank (UKBB) Resource under
 542 Application Number xxxx. All datasets are de-identified and contain no personally identifiable infor-
 543 mation. No direct human subject recruitment was involved, and the work does not raise foreseeable
 544 risks to participants.

545 **Reproducibility Statement:** We provide detailed descriptions of datasets, preprocessing steps,
 546 model architectures, training procedures, and evaluation protocols in Sec. 3 and Sec. 4 of the
 547 manuscript and Appendix B to ensure reproducibility of our model and compared approaches.
 548 Source code and model weights will be made publicly available at <https://github.com/anonymous> upon acceptance.
 549

550 **LLM Usage:** We note that large language models (LLMs) were used solely to improve language
 551 clarity; all scientific content and ideas were developed by the authors.
 552

553 **REFERENCES**

555 Julián N Acosta, Guido J Falcone, Pranav Rajpurkar, and Eric J Topol. Multimodal biomedical AI.
 556 *Nature Medicine*, 2022.

558 Tadas Baltrušaitis, Chaitanya Ahuja, and Louis-Philippe Morency. Multimodal machine learning:
 559 A survey and taxonomy. *IEEE TPAMI*, 2018.

560 Arindam Banerjee, Srujana Merugu, Inderjit S Dhillon, and Joydeep Ghosh. Clustering with breg-
 561 man divergences. *JMLR*, 2005.

563 Bing Cao, Yinan Xia, Yi Ding, Changqing Zhang, and Qinghua Hu. Predictive dynamic fusion. In
 564 *ICML*. PMLR, 2024.

565 Ting Chen, Simon Kornblith, Mohammad Norouzi, and Geoffrey Hinton. A simple framework for
 566 contrastive learning of visual representations. In *ICML*. PMLR, 2020.

568 Thomas M Cover. *Elements of information theory*. John Wiley & Sons, 1999.

569 Yinglong Dai, Zheng Yan, Jiangchang Cheng, Xiaojun Duan, and Guojun Wang. Analysis of mul-
 570 timodal data fusion from an information theory perspective. *Information Sciences*, 2023.

572 Jacob Devlin, Ming-Wei Chang, Kenton Lee, and Kristina Toutanova. BERT: Pre-training of deep
 573 bidirectional transformers for language understanding. In *ACL*, 2019.

574 Siyi Du, Shaoming Zheng, Yinsong Wang, Wenjia Bai, Declan P O'Regan, and Chen Qin.
 575 TIP: Tabular-image pre-training for multimodal classification with incomplete data. In *ECCV*.
 576 Springer, 2024.

578 Siyi Du, Xinzhe Luo, Declan P O'Regan, and Chen Qin. STiL: Semi-supervised tabular-image
 579 learning for comprehensive task-relevant information exploration in multimodal classification. In
 580 *CVPR*, 2025.

581 Jiafei Duan, Samson Yu, Hui Li Tan, Hongyuan Zhu, and Cheston Tan. A survey of embodied
 582 AI: From simulators to research tasks. *IEEE Transactions on Emerging Topics in Computational*
 583 *Intelligence*, 2022.

584 William Fedus, Barret Zoph, and Noam Shazeer. Switch transformers: Scaling to trillion parameter
 585 models with simple and efficient sparsity. *JMLR*, 2022.

587 Xin Gao and Jian Pu. Deep incomplete multi-view learning via cyclic permutation of VAEs. In
 588 *ICLR*, 2025.

589 Zixian Gao, Xun Jiang, Xing Xu, Fumin Shen, Yujie Li, and Heng Tao Shen. Embracing unimodal
 590 aleatoric uncertainty for robust multimodal fusion. In *CVPR*, 2024.

592 Jifeng Guo, CL Philip Chen, Zhulin Liu, and Xixin Yang. Dynamic neural network structure: A
 593 review for its theories and applications. *IEEE Transactions on Neural Networks and Learning*
 594 *Systems*, 2024.

594 Paul Hager, Martin J Menten, and Daniel Rueckert. Best of both worlds: Multimodal contrastive
 595 learning with tabular and imaging data. In *CVPR*, 2023.

596

597 Yizeng Han, Gao Huang, Shiji Song, Le Yang, Honghui Wang, and Yulin Wang. Dynamic neural
 598 networks: A survey. *IEEE TPAMI*, 2021.

599

600 Martin Heusel, Hubert Ramsauer, Thomas Unterthiner, Bernhard Nessler, and Sepp Hochreiter.
 601 GANs trained by a two time-scale update rule converge to a local nash equilibrium. *NIPS*, 2017.

602

603 Wassily Hoeffding. Probability inequalities for sums of bounded random variables. *Journal of the
 American Statistical Association*, 1963.

604

605 Jingmin Huang, Bowei Chen, Lan Luo, et al. DVM-CAR: A large-scale automotive dataset for
 606 visual marketing research and applications. In *2022 IEEE International Conference on Big Data
 (Big Data)*. IEEE, 2022a.

607

608 Yu Huang, Junyang Lin, Chang Zhou, Hongxia Yang, and Longbo Huang. Modality competition:
 609 What makes joint training of multi-modal network fail in deep learning?(provably). In *ICML*.
 610 PMLR, 2022b.

611

612 Ian Jolliffe. Principal component analysis. In *International encyclopedia of statistical science*.
 Springer, 2011.

613

614 Diederik P Kingma and Jimmy Ba. ADAM: A method for stochastic optimization. *arXiv preprint
 arXiv:1412.6980*, 2014.

615

616 Yi-Lun Lee, Yi-Hsuan Tsai, Wei-Chen Chiu, and Chen-Yu Lee. Multimodal prompting with missing
 617 modalities for visual recognition. In *CVPR*, 2023.

618

619 Junnan Li, Caiming Xiong, and Steven CH Hoi. CoMatch: Semi-supervised learning with con-
 620 trastive graph regularization. In *ICCV*, 2021.

621

622 Sijie Li, Chen Chen, and Jungong Han. SimMLM: A simple framework for multi-modal learning
 with missing modality. In *ICCV*, 2025.

623

624 Jingchen Liu, Andrew Gelman, Jennifer Hill, Yu-Sung Su, and Jonathan Kropko. On the stationary
 625 distribution of iterative imputations. *Biometrika*, 2014.

626

627 Qidong Liu, Jiaxi Hu, Yutian Xiao, Xiangyu Zhao, Jingtong Gao, Wanyu Wang, Qing Li, and Jiliang
 Tang. Multimodal recommender systems: A survey. *ACM Computing Surveys*, 2024.

628

629 Chao Ma, Sebastian Tschiatschek, Konstantina Palla, Jose Miguel Hernandez-Lobato, Sebastian
 630 Nowozin, and Cheng Zhang. EDDI: Efficient dynamic discovery of high-value information with
 631 partial vae. In *ICML*. PMLR, 2019.

632

633 Mengmeng Ma, Jian Ren, Long Zhao, Sergey Tulyakov, Cathy Wu, and Xi Peng. SMIL: Multimodal
 learning with severely missing modality. In *AAAI*, 2021.

634

635 Mengmeng Ma, Jian Ren, Long Zhao, Davide Testuggine, and Xi Peng. Are multimodal transfor-
 636 mers robust to missing modality? In *CVPR*, 2022.

637

638 Yingyao Ma, Yifan Xue, Jiasong Wu, Lotfi Senhadji, Huazhong Shu, and Jian Yang. Multimodal en-
 639 tity linking with dynamic modality selection and interactive prompt learning. *IEEE Transactions
 on Knowledge and Data Engineering*, 2025.

640

641 Laurens van der Maaten and Geoffrey Hinton. Visualizing data using t-SNE. *JMLR*, 2008.

642

643 Mehryar Mohri, Afshin Rostamizadeh, and Ameet Talwalkar. *Foundations of machine learning*.
 MIT press, 2018.

644

645 Natalia Neverova, Christian Wolf, Graham Taylor, and Florian Nebout. ModDrop: adaptive multi-
 646 modal gesture recognition. *IEEE TPAMI*, 2015.

647

Jiquan Ngiam, Aditya Khosla, Mingyu Kim, Juhan Nam, Honglak Lee, Andrew Y Ng, et al. Multi-
 modal deep learning. In *ICML*, 2011.

648 Emanuele Palumbo, Imant Daunhawer, and Julia E Vogt. MMVAE+: Enhancing the generative
 649 quality of multimodal vaes without compromises. In *ICLR*. OpenReview, 2023.
 650

651 Emanuele Palumbo, Laura Manduchi, Sonia Laguna Cillero, Daphné Chopard, and Julia E Vogt.
 652 Deep generative clustering with multimodal diffusion variational autoencoders. In *ICLR*. Open-
 653 Review, 2024.

654 Yuntao Shou, Jun Yao, Tao Meng, Wei Ai, Cen Chen, and Keqin Li. GSDNet: Revisiting incomplete
 655 multimodality-diffusion emotion recognition from the perspective of graph spectrum. In *IJCAI*,
 656 2025.

657

658 Jake Snell, Kevin Swersky, and Richard Zemel. Prototypical networks for few-shot learning. *NIPS*,
 659 2017.

660 Cathie Sudlow, John Gallacher, Naomi Allen, Valerie Beral, Paul Burton, et al. UK Biobank: an
 661 open access resource for identifying the causes of a wide range of complex diseases of middle
 662 and old age. *PLoS Medicine*, 2015.

663

664 Thomas Sutter, Imant Daunhawer, and Julia Vogt. Multimodal generative learning utilizing jensen-
 665 shannon-divergence. *NIPS*, 2020.

666

667 Thomas M Sutter, Imant Daunhawer, and Julia E Vogt. Generalized multimodal ELBO. In *ICLR*,
 668 2021.

669

670 Naftali Tishby and Noga Zaslavsky. Deep learning and the information bottleneck principle. In
 671 *2015 IEEE Information Theory Workshop (ITW)*. IEEE, 2015.

672

673 Ashish Vaswani, Noam Shazeer, Niki Parmar, Jakob Uszkoreit, Llion Jones, Aidan N Gomez,
 674 Łukasz Kaiser, and Illia Polosukhin. Attention is all you need. *NIPS*, 2017.

675

676 Oriol Vinyals, Charles Blundell, Timothy Lillicrap, Daan Wierstra, et al. Matching networks for one
 677 shot learning. *NIPS*, 2016.

678

679 Hu Wang, Yuanhong Chen, Congbo Ma, Jodie Avery, Louise Hull, and Gustavo Carneiro. Multi-
 680 modal learning with missing modality via shared-specific feature modelling. In *CVPR*, 2023a.

681

682 Yuanzhi Wang, Yong Li, and Zhen Cui. Incomplete multimodality-diffused emotion recognition.
 683 *NIPS*, 2023b.

684

685 Shicai Wei, Chunbo Luo, and Yang Luo. MMANet: Margin-aware distillation and modality-aware
 686 regularization for incomplete multimodal learning. In *CVPR*, 2023.

687

688 Sangmin Woo, Sumin Lee, Yeonju Park, Muhammad Adi Nugroho, and Changick Kim. Towards
 689 good practices for missing modality robust action recognition. In *AAAI*, 2023.

690

691 Renjie Wu, Hu Wang, Hsiang-Ting Chen, and Gustavo Carneiro. Deep multimodal learning with
 692 missing modality: A survey. *arXiv preprint arXiv:2409.07825*, 2024a.

693

694 Zhenbang Wu, Anant Dadu, Nicholas Tustison, Brian Avants, Mike Nalls, Jimeng Sun, and Faraz
 695 Faghri. Multimodal patient representation learning with missing modalities and labels. In *ICLR*,
 696 2024b.

697

698 Yingxue Xu, Fengtao Zhou, Chenyu Zhao, Yihui Wang, Can Yang, and Hao Chen. Distilled prompt
 699 learning for incomplete multimodal survival prediction. In *CVPR*, 2025.

700

701 Chonghua Xue, Sahana S Kowshik, Diala Lteif, Shreyas Puducher, Varuna H Jasodanand, Olivia T
 702 Zhou, Anika S Walia, Osman B Guney, J Diana Zhang, Serena Poésy, et al. AI-based differential
 703 diagnosis of dementia etiologies on multimodal data. *Nature Medicine*, 2024.

704

705 Zihui Xue and Radu Marculescu. Dynamic multimodal fusion. In *CVPRW*, 2023.

706

707 Weiyi Yang, Richong Zhang, Junfan Chen, Lihong Wang, and Jaein Kim. Prototype-guided pseudo
 708 labeling for semi-supervised text classification. In *ACL*, 2023.

702 Yang Yue, Yulin Wang, Bingyi Kang, Yizeng Han, Shenzhi Wang, Shiji Song, Jiashi Feng, and Gao
703 Huang. Deer-VLA: Dynamic inference of multimodal large language models for efficient robot
704 execution. *NIPS*, 2024.

705
706 Yifan Zhan, Rui Yang, Junxian You, Mengjie Huang, Weibo Liu, and Xiaohui Liu. A systematic
707 literature review on incomplete multimodal learning: techniques and challenges. *Systems Science*
708 & *Control Engineering*, 2025.

709 Chaohe Zhang, Xu Chu, Liantao Ma, Yinghao Zhu, Yasha Wang, Jiangtao Wang, and Junfeng Zhao.
710 M3Care: Learning with missing modalities in multimodal healthcare data. In *ACM SIGKDD*,
711 2022.

712
713 Qingyang Zhang, Haitao Wu, Changqing Zhang, Qinghua Hu, Huazhu Fu, Joey Tianyi Zhou, and
714 Xi Peng. Provable dynamic fusion for low-quality multimodal data. In *ICML*. PMLR, 2023.

715
716 Qingyang Zhang, Yake Wei, Zongbo Han, Huazhu Fu, Xi Peng, Cheng Deng, Qinghua Hu, Cai Xu,
717 Jie Wen, Di Hu, et al. Multimodal fusion on low-quality data: A comprehensive survey. *arXiv
preprint arXiv:2404.18947*, 2024.

718
719 Tong Zhang, Shu Shen, and CL Chen. MICINet: Multi-level inter-class confusing information
720 removal for reliable multimodal classification. *arXiv preprint arXiv:2502.19674*, 2025.

721

722

723

724

725

726

727

728

729

730

731

732

733

734

735

736

737

738

739

740

741

742

743

744

745

746

747

748

749

750

751

752

753

754

755

756 Appendices

759 **Overview:** The appendices are structured to provide further details and supporting evidence for
 760 the manuscript. In Appendix A, we provide the detailed formulations of the proposed DyMo. Ap-
 761 pendix B describes the datasets used in our experiments, together with the implementation details for
 762 both DyMo and the baseline algorithms to ensure reproducibility. Finally, Appendix C presents ad-
 763 ditional experiments, including the complete results under various missing-data scenarios, extended
 764 ablation studies, generalization analysis (*e.g.*, evaluating robustness across different modality recov-
 765 ery methods), adaptive inference analysis, additional visualizations, and reconstruction performance
 766 evaluation of modality recovery methods.

767 A DETAILED FORMULATION

768 A.1 RELATIONSHIP BETWEEN TASK LOSS FUNCTION & TASK-RELEVANT INFORMATION

769 Our dynamic selection algorithm leverages a novel multimodal task-relevant information reward
 770 (MTIR) to rank the incremental multimodal task-relevant information gained from adding each re-
 771 covered modality. Since the underlying data distribution is unknown at inference time, we introduce
 772 a tractable proxy based on the task (*i.e.*, classification) loss function. In this section, we derive the
 773 connection between task loss and task-relevant information, demonstrating that reducing the task
 774 loss can increase the lower bound on task-relevant information.

775 Let the true conditional distribution of labels given representations be $p(y|z)$, and the model-
 776 predicted distribution be $q_\theta(y|z)$, where θ denotes model parameters, y is the classification label,
 777 and z is the multimodal representation. The true classification cross-entropy (CE) loss over a test
 778 dataset \mathcal{D} is:

$$779 \mathcal{L}_{\text{ce}} = \text{CE}(p(y|z); q_\theta(y|z)) \\ 780 = - \int_z p(z) \left[\int_y p(y|z) \log q_\theta(y|z) dy \right] dz. \quad (\text{S1})$$

781 We can decompose the cross-entropy into conditional entropy and conditional KL divergence:

$$782 \mathcal{L}_{\text{ce}} = - \int_z p(z) \left[\int_y p(y|z) \log q_\theta(y|z) dy \right] dz + \int_z p(z) \left[\int_y p(y|z) \log p(y|z) dy \right] dz - \int_z p(z) \left[\int_y p(y|z) \log p(y|z) dy \right] dz \\ 783 = - \int_z p(z) \left[\int_y p(y|z) \log p(y|z) dy \right] dz + \int_z p(z) \left[\int_y p(y|z) \log \frac{p(y|z)}{q_\theta(y|z)} \right] dz \\ 784 = H(Y|Z) + \text{KL}(p(y|z) || q_\theta(y|z)). \quad (\text{S2})$$

785 Since conditional KL divergence is non-negative (Cover, 1999), we have

$$786 \mathcal{L}_{\text{ce}} \geq H(Y|Z). \quad (\text{S3})$$

787 On the other hand, the task-relevant information contained in multimodal representations Z can be
 788 quantified by the mutual information between Z and the labels Y (Tishby & Zaslavsky, 2015):

$$789 I(Y; Z) = \mathbb{E}_{p(y,z)} \log \frac{p(y,z)}{p(y)p(z)} \\ 790 = -\mathbb{E}_{p(y,z)} \log p(y) + \mathbb{E}_{p(y,z)} \log p(y|z) \\ 791 = H(Y) - H(Y|Z), \quad (\text{S4})$$

800 where $H(Y)$ is the entropy of labels. Combining this with Eq. S3 yields a lower bound on mutual
 801 information:

$$802 I(Y; Z) \geq H(Y) - \mathcal{L}_{\text{ce}} \quad (\text{S5})$$

803 This shows that the lower bound on mutual information increases as the [expected](#) CE loss \mathcal{L}_{ce} de-
 804 creases, motivating the use of the loss as a tractable proxy for task-relevant information. In practice,
 805 since the true distributions $p(z)$ and $p(y|z)$ are unknown, we estimate the bound using the empirical
 806 [test](#) CE loss computed from one-hot labels. The empirical [test](#) CE loss is written as:

$$807 \hat{\mathcal{L}}_{\text{ce}} = \frac{1}{|\mathcal{D}|} \sum_{j=1}^{|\mathcal{D}|} \ell_{\text{ce}_j} = \frac{1}{|\mathcal{D}|} \sum_{j=1}^{|\mathcal{D}|} -\log q_\theta(y_j|z_j). \quad (\text{S6})$$

810 Assuming that the model is well-trained, we follow the common bounded-loss assumption in prior
 811 work that the per-sample CE loss is bounded in practice (Cao et al., 2024; Zhang et al., 2023; Mohri
 812 et al., 2018). Therefore, we adopt a conservative bound:

$$813 \quad 0 \leq \ell_{\text{ce}_j} = -\log q_{\theta}(y_j | \mathbf{z}_j) \leq G, \quad \forall j \in \{1, 2, \dots, |\mathcal{D}|\}. \quad (S7)$$

814 Then, by Hoeffding's inequality (Hoeffding, 1963), with probability at least $1 - \delta$,

$$815 \quad \mathcal{L}_{\text{ce}} \leq \hat{\mathcal{L}}_{\text{ce}} + G \sqrt{\frac{\ln(1/\delta)}{2|\mathcal{D}|}}. \quad (S8)$$

816 Substituting this into Eq. S5, we obtain a high-probability lower bound on the mutual information
 817 in terms of the empirical test CE loss:

$$818 \quad I(Y; \mathbf{Z}) \geq H(Y) - \hat{\mathcal{L}}_{\text{ce}} - G \sqrt{\frac{\ln(1/\delta)}{2|\mathcal{D}|}}, \quad \text{with probability at least } 1 - \delta. \quad (S9)$$

819 In this equation, the last term $G \sqrt{\frac{\ln(1/\delta)}{2|\mathcal{D}|}}$ is constant and will be nearly to zero when the test dataset
 820 size is sufficient large. Therefore, reducing the empirical test CE loss can increase the lower bound
 821 on task-relevant information contained in multimodal representations \mathbf{z} , which provides the theoretical
 822 foundation of our MTIR reward in the dynamic modality selection algorithm.

823 A.2 FORMULATION ON THE FEATURE SPACE

824 A regular Bregman divergence (Banerjee et al., 2005) d_{ϕ} is defined as:

$$825 \quad d_{\phi}(\mathbf{z}, \mathbf{z}') = \phi(\mathbf{z}) - \phi(\mathbf{z}') - (\mathbf{z} - \mathbf{z}')^T \nabla_{\phi}(\mathbf{z}'), \quad (S10)$$

826 where ϕ is a differentiable, strictly convex function of the Legendre type, e.g., squared Euclidean
 827 distance or Mahalanobis distance. Inspired by prototypical networks (Snell et al., 2017), the poste-
 828 rior probability $p(y|\mathbf{z})$ can be interpreted as a mixture density estimation on the training set with an
 829 exponential family density defined in the feature space.

830 Any regular exponential family distribution $p_{\Psi}(\mathbf{z}, \boldsymbol{\theta})$ with natural parameters $\boldsymbol{\theta}$ and cumulant func-
 831 tion Ψ can be written in terms of a uniquely determined regular Bregman divergence:

$$832 \quad p_{\Psi}(\mathbf{z}|\boldsymbol{\theta}) = \exp(\langle \mathbf{z}, \boldsymbol{\theta} \rangle - \Psi(\boldsymbol{\theta})) p_0(\mathbf{z}) = \exp(-d_{\phi}(\mathbf{z}, \boldsymbol{\mu}(\boldsymbol{\theta}))) b_{\phi}(\mathbf{z}), \quad (S11)$$

833 where $b_{\phi}(\mathbf{z}) = \exp(\phi(\mathbf{z})) p_0(\mathbf{z})$ and $\boldsymbol{\mu}(\boldsymbol{\theta})$ is the mean parameter. Consider a regular exponential
 834 family mixture model with parameters $\Gamma = \{\boldsymbol{\theta}_k, \pi_k\}_{k=1}^K$:

$$835 \quad p(\mathbf{z}|\Gamma) = \sum_{k=1}^K \pi_k p_{\Psi}(\mathbf{z}|\boldsymbol{\theta}_k) = \sum_{k=1}^K \pi_k \exp(-d_{\phi}(\mathbf{z}, \boldsymbol{\mu}(\boldsymbol{\theta}_k))) b_{\phi}(\mathbf{z}). \quad (S12)$$

836 Given Γ , the posterior probability of assigning an unlabeled data point \mathbf{z} to cluster k is:

$$837 \quad p(y=k|\mathbf{z}) = \frac{p(y=k)p(\mathbf{z}|y=k)}{p(\mathbf{z}|\Gamma)} = \frac{\pi_k \exp(-d_{\phi}(\mathbf{z}, \boldsymbol{\mu}(\boldsymbol{\theta}_k)))}{\sum_{k'=1}^K \pi_{k'} \exp(-d_{\phi}(\mathbf{z}, \boldsymbol{\mu}(\boldsymbol{\theta}_{k'})))} \quad (S13)$$

838 Following Snell et al. (2017), we assume an equally-weighted mixture model with one cluster per
 839 class, where $\pi_k = \frac{1}{K}$, and $\boldsymbol{\mu}(\boldsymbol{\theta}_k) = \mathbf{c}_k$ denotes the class prototype estimated from the training data.
 840 The posterior probability then simplifies to:

$$841 \quad p(y=k|\mathbf{z}) = \frac{\exp(-d_{\phi}(\mathbf{z}, \mathbf{c}_k))}{\sum_{k'=1}^K \exp(-d_{\phi}(\mathbf{z}, \mathbf{c}_{k'}))}, \quad \mathbf{c}_k = \frac{1}{\sum_{i=1}^N \mathbb{I}[y_i=k]} \sum_{i:y_i=k} \mathbf{z}_i. \quad (S14)$$

842 During training, we utilize the class prototypes to calculate our auxiliary missing-agnostic
 843 contrastive loss L_{aux} . To avoid storing instance embeddings, we maintain the cumulative sum of em-
 844 beddings and sample counts for each class during training and compute the prototype at the end of
 845 each epoch.

Note that the representations of a sample may differ across different modality subsets. To account for this, at inference time, we further define subset-specific class prototypes. In specific, for each class $k \in \{1, \dots, K\}$ and each non-empty modality subset $\mathcal{S} \subseteq [M], \mathcal{S} \neq \emptyset$, we construct:

$$\mathbf{c}_{k,\mathcal{S}} = \frac{1}{\sum_{i=1}^N \mathbb{I}[y_i = k]} \sum_{i:y_i=k} \psi\left(h\left(\{\mathbf{x}_i^{(m)}\}_{m \in \mathcal{S}}\right)\right), \quad (\text{S15})$$

where h denotes modality-specific encoders and ψ is the multimodal transformer (notations follow Sec. 3.1). We then aggregate these prototypes into an averaged class prototype by considering all possible non-empty modality subsets:

$$\bar{\mathbf{c}}_k = \frac{1}{2^M - 1} \sum_{\mathcal{S} \subseteq [M], \mathcal{S} \neq \emptyset} \mathbf{c}_{k,\mathcal{S}}. \quad (\text{S16})$$

In practice, $\bar{\mathbf{c}}_k$ is substituted for \mathbf{c}_k in Eq. S14. For the ICS score calculation of a sample representation \mathbf{z} , we apply its associated modality subset \mathcal{S} to all training samples and compute Eq. 8 using these subset-specific representations.

In our experiments, we evaluated two common distance metrics: the squared Euclidean distance and the cosine distance. While cosine distance does not strictly belong to the class of Bregman divergences, it is widely used in high-dimensional embedding spaces, where directional similarity is often more informative than vector magnitude (Li et al., 2021; Yang et al., 2023; Du et al., 2025). Our experimental results demonstrate that cosine distance achieves performance comparable to Bregman divergences, suggesting its suitability as a metric for our modality selection algorithm.

B DATASET AND IMPLEMENTATION DETAILS

B.1 DETAILED DATA DESCRIPTION

As summarized in Tab. S1, we conduct extensive experiments on 5 datasets with diverse modalities, *e.g.*, image, text, and structured tables. These comprises of 3 simulated benchmark datasets (Sutter et al., 2021; 2020): PolyMNIST, MNIST-SVHN-Text (MST), and biomodal CelebA (CelebA), as well as two large real-world datasets: a natural image dataset, Data Visual Marketing (DVM) (Huang et al., 2022a) and a medical image dataset, UK Biobank (UKBB) (Sudlow et al., 2015).

PolyMNIST consists of 5 images per data point, all sharing the same digit label but with different backgrounds and handwriting styles. MST is a trimodal dataset combining MNIST, street view house numbers (SVHN), and synthetic text features. CelebA contains facial images paired with descriptive text annotations of facial attributes. The DVM dataset includes 2D RGB images of cars along with tabular data describing vehicle characteristics. Following (Du et al., 2024; Hager et al., 2023; Du et al., 2025), we used 17 tabular features, including 4 categorical features (*e.g.*, color), and 13 continuous features (*e.g.*, width). The UKBB dataset consists of cardiac magnetic resonance images (MRIs) accompanied by tabular data related to cardiovascular diseases. Following prior work (Hager et al., 2023), we used mid-ventricle slices from MRIs at three time points, *i.e.*, end-systolic (ES) frame, end-diastolic (ED) frame, and an intermediate time frame between ED and ES. In addition, we employed 75 disease-related tabular features, including 26 categorical features (*e.g.*, alcohol drinker status) and 49 continuous features (*e.g.*, average heart rate). Notably, due to low disease prevalence, similar to (Du et al., 2025), we constructed 2 balanced training subsets for CAD and Infarction tasks, respectively. Detailed benchmark information for DVM and UKBB, including the complete list of tabular feature names, can be found in the supplementary material of (Du et al., 2024).

B.2 IMPLEMENTATION DETAILS

For both DVM and UKBB, we adopted the data augmentation strategies described in (Hager et al., 2023; Du et al., 2024). For image data, we applied random scaling, rotation, shifting, flipping, Gaussian noise, as well as brightness, saturation, and contrastive changes, followed by resizing all images to 128×128 . For tabular data, categorical values (*e.g.*, yes, no, and blue) were converted into ordinal integers, while continuous (numerous) values were standardized using z -score normalization. To further enhance data diversity, we randomly replaced 30% of the tabular values for each subject

918

919

Table S1: Summary of the 5 multimodal datasets for evaluation.

Dataset	Classification Task	#Modality	Modality Type	#Train	#Val	#Test	#Class
PolyMNIST	Digit	5	RGB image	60,000	3,000	7,000	10
MST	Digit	3	RGB image, Text	1,121,360	60,000	140,000	10
CelebA	Face attribute	2	RGB image, Text	162,770	19,962	19,867	2
DVM	Car model	2	RGB image, Table	70,565	17,642	88,207	283
UKBB	Coronary artery disease (CAD)	2	MR image, Table	3,482	6,510	3,617	2
	Myocardial infarction	2	MR image, Table	1,552	6,510	3,617	2

920

921

922

923

924

925

926

927

Table S2: Hyper-parameter configurations for DyMo.

Hyper-parameter	PolyMNIST	MST	CelebA	DVM	CAD	Infarction
# layers of the multimodal transformer	2	2	2	2	2	2
# attention heads of the multimodal transformer	4	2	2	8	8	8
Hidden dimension of the multimodal transformer	128	32	32	256	256	256
Sequence length per modality	{4,4,4,4,4}	{1,1,1}	{1,1}	{I:16,T:17}	{I:16,T:75}	{I:16,T:75}
Latent space dimension	64	16	16	128	128	128
# sampled modality subsets (A)	5	2	2	2	2	2
Learning rate	1e-3	1e-3	1e-3	3e-4	3e-4	3e-4
Batch size	256	256	256	256	128	128
Maximum # epochs	100	20	20	300	300	300

928

929

930

931

932

933

934

935

936

937

938

939

940

with randomly sampled values from the corresponding columns. Hyper-parameter settings for the proposed DyMo and all compared approaches are detailed below.

941

Our DyMo: For the recovery method in DyMo, we leveraged MoPoE (Sutter et al., 2021), a multimodal VAE, for PolyMNIST, MST, and CelebA. For DVM and UKBB, we used TIP (Du et al., 2024), an image-tabular framework capable of reconstructing tabular features from images and incomplete tables. Importantly, DyMo is agnostic to the choice of recovery method and can be deployed with any recovery method. For modality-specific encoders, as done in (Sutter et al., 2021), we used convolutional neural networks (CNNs) for images and multi-layer perceptrons (MLPs) for text in PolyMNIST, MST, and CelebA. For DVM and UKBB, we followed (Du et al., 2024), using ResNet-50 as the image encoder and a transformer-based encoder for tabular data. The tabular encoder consists of 4 transformer layers, each with 8 attention heads and a hidden dimension of 512. To ensure fairness, all comparing approaches employed the same encoders as DyMo. To mitigate the curse of dimensionality, multimodal representations z were projected into a low-dimensional latent space using a 2-layer MLP before distance computation. The temperature parameter t for distance metrics was set to 0.1. Hyper-parameter configurations for DyMo are summarized in Tab. S2.

942

943

944

945

946

947

948

949

950

951

952

953

954

955

956

957

CONCAT (Baltrušaitis et al., 2018): This static fusion algorithm has been widely adopted in MDL tasks due to its simplicity and effectiveness. CONCAT concatenates modality-specific features into a unified multimodal representation, which is then used for the classification task.

958

959

960

961

962

963

964

965

966

967

968

QMF (Zhang et al., 2023): This dynamic MDL framework performs modality fusion through uncertainty-aware weighing. Modality-specific uncertainty is estimated via an energy score computed from the output logits of each unimodal network. In addition, QMF incorporates a regularization loss based on the historical training trajectory. Following the original paper, the number of gradient accumulation steps was set to 12 for CAD and Infarction, and 24 for the remaining tasks.

969

970

971

DynMM (Xue & Marculescu, 2023): This dynamic MDL approach employs a learnable gating network. Given M modalities, it constructs $M + 1$ network branches: M modality-specific networks and one concatenation-based multimodal network. The gating network adaptively selects one branch for decision-making. Note that this approach requires two-stage training: (i) pre-training each network branch independently on the target task, and (ii) jointly fine-tuning all network branches together with the gating network.

972

973

974

PDF (Cao et al., 2024): This dynamic MDL framework introduces a modality confidence score to fuse unimodal predictions. The score is derived from the predicted class probability of each unimodal network. In addition, to address potential uncertainty, a relative calibration strategy is further applied to calibrate the confidence scores.

972 **MultiAE (Ngiam et al., 2011):** This incomplete MDL model is an offline recovery-based method.
 973 It first pre-trains a multimodal autoencoder (AE) with a reconstruction objective, then freezes the
 974 AE encoder and uses the extracted latent features to train a classifier for downstream tasks. Since the
 975 original design does not simulate missing modalities during training, we incorporated our incom-
 976 plete simulation training to obtain MultiAE[†]. The hyper-parameter settings of this strategy were
 977 aligned with our DyMo (see Tab. S2). The number of pre-training epochs was set to 300 for PolyM-
 978 NIST and 200 for MST and CelebA. The same learning rate was used for both pre-training and
 979 fine-tuning, matching the learning rate used by DyMo in its one-stage training.

980 **MoPoE (Sutter et al., 2021):** This incomplete MDL approach is also offline recovery-based. It
 981 first pre-trains a multimodal VAE with an ELBO formulation tailored for incomplete multimodal
 982 data. The encoder is then frozen, and its extracted latent features are used to train a classifier for
 983 downstream tasks. Pre-training was performed for 100 epochs, and the learning rates for pre-training
 984 and fine-tuning were identical, equal to that used by DyMo.

985 **M3Care (Zhang et al., 2022):** This incomplete MDL framework is an online recovery-based
 986 method. It imputes missing modality information in the latent space using auxiliary information
 987 from similar patents, identified via a task-guided, modality-adaptive similarity metric. Since the
 988 original design does not simulate modality missing during training, we incorporated our incom-
 989 plete simulation training to obtain M3Care[†]. The hyper-parameter settings of this strategy were aligned
 990 with our DyMo.

991 **OnlineMAE (Woo et al., 2023):** This incomplete MDL model is an online recovery-based method.
 992 It jointly optimizes a feature-level reconstruction task and the target classification task by randomly
 993 dropping modality features and reconstructing them from the remaining modalities. In reproduction,
 994 we observed that training from scratch often led to model collapse, likely because the network
 995 initially fails to extract reliable features, making feature-level reconstruction unstable. To mitigate
 996 this, we initialized the encoders with weights from MultiAE (after downstream task training) for
 997 PolyMNIST, MST, and CelebA, and weights from TIP (after downstream task training) for DVM,
 998 CAD, and Infarction.

999 **ModDrop (Neverova et al., 2015):** This incomplete MDL framework is a missing-agnostic,
 1000 recovery-free method. It applies random modality dropping during target task training to encourage
 1001 modality-agnostic representation learning. Each modality is dropped according to a Bernoulli distri-
 1002 bution with probability p . For a fair comparison, we used the same multimodal network architecture
 1003 as our DyMo. Following the original paper, p was set to 0.5.

1004 **MTL (Ma et al., 2022):** This incomplete MDL model is a missing-aware, recovery-free method. It
 1005 introduces a multimodal transformer architecture with missing-aware [CLS] tokens, which encode
 1006 different missing patterns. Attention masks on those [CLS] tokens ensure that they only aggregate
 1007 information from observed modalities. To optimize missingness-specific parameters, a multi-task
 1008 learning strategy is used to compute loss across all missing patterns in each training step. The
 1009 sequence length per modality and transformer configurations matched those of our DyMo.

1010 **MAP (Lee et al., 2023):** This incomplete MDL approach is also missing-aware and recovery-free.
 1011 It designs a multimodal transformer architecture with missing-aware prompts. Prompts are assigned
 1012 based on the missing pattern of each input and injected into multiple transformer blocks. Since
 1013 the original paper does not simulate missing modalities during training, we applied our incom-
 1014 plete simulation training to obtain MAP[†]. The sequence length per modality and transformer configura-
 1015 tions followed those of our DyMo. Following the original paper, prompt lengths were set to 12 for
 1016 PolyMNIST, 2 for MST and CelebA, 8 for DVM, and 16 for CAD and Infarction. Prompts were
 1017 applied to 2 transformer layers.

1018 **MUSE (Wu et al., 2024b):** This incomplete MDL framework is a missing-agnostic, recovery-
 1019 free method. It models patient-modality relationships using a flexible bipartite graph that supports
 1020 arbitrary missing-modality patterns. The vertex set includes patient nodes and modality nodes, and
 1021 edges are defined by the modality missingness matrix. To learn modality-agnostic features, a mutual-
 1022 consistent contrastive loss is applied, where each edge is dropped with probability p . Following the
 1023 original paper, p was set to 0.5.

1024 We trained all models using the Adam optimizer (Kingma & Ba, 2014) without weight decay and ran
 1025 experiments on a single NVIDIA A5000 GPU. To mitigate overfitting, similar to (Du et al., 2024;

1026

1027 Table S3: Complete results on PolyMNIST and MST under various missing scenarios, comparing
 1028 DyMo with incomplete MDL methods, including both recovery-based and recovery-free ap-
 1029 proaches. Models marked with \dagger were trained using our proposed incomplete-modality sim-
 1030 ulation training. In addition to the results reported in Tab. 1, we also include PolyMNIST results for
 1031 $\eta = \{0.2, 0.4\}$ and MST results for missing modality subsets $\{\text{M}\}$, $\{\text{S}\}$, $\{\text{T}\}$, and $\{\text{M}, \text{S}\}$.

Model	Publication	PolyMNIST Acc (%) \uparrow					MST Acc (%) \uparrow							
		Missing Rate η					Missing Modality/ies							
			0	0.2	0.4	0.6	0.8	{}	{M}	{S}	{T}	{M,S}	{S,T}	{M,T}
(a) Recovery-based Methods for Missing Modality														
MultiAE	ICML'11	99.77	99.39	98.56	95.36	84.39	99.96	99.74	99.98	98.30	100	97.00	81.60	
MultiAE \dagger	ICML'11	99.94	99.83	99.03	97.50	89.86	99.87	98.65	99.93	98.60	100	98.33	83.44	
MoPoE	ICLR'21	99.79	99.41	98.13	93.94	79.84	99.62	91.32	99.33	92.28	<u>90.11</u>	90.86	79.01	
MoPoE \dagger	ICLR'21	99.63	99.57	98.96	96.81	87.06	99.39	99.42	99.18	97.62	100	96.50	82.54	
CMVAE	ICLR'24	94.93	95.50	95.21	95.13	95.11	-	-	-	-	-	-	-	
CMVAE \dagger	ICLR'24	94.59	95.23	94.93	95.17	95.20	-	-	-	-	-	-	-	
M3Care	KDD'22	99.93	89.26	74.93	56.66	40.53	<u>99.99</u>	40.64	85.18	23.48	41.69	16.03	9.34	
M3Care \dagger	KDD'22	<u>99.99</u>	<u>99.93</u>	99.40	97.27	87.92	99.98	100	99.98	<u>99.17</u>	100	98.27	85.16	
OnlineMAE	AAAI'23	100	99.89	<u>99.61</u>	98.29	90.09	99.90	99.70	99.96	97.94	100	98.14	84.14	
(b) Recovery-free Methods for Missing Modality														
ModDrop	ICML'15	99.97	99.77	99.43	97.66	88.44	100	100	100	99.14	100	98.21	82.47	
MTL	CVPR'22	99.97	99.91	<u>99.61</u>	98.43	91.14	99.96	99.97	99.96	98.82	100	98.60	84.37	
MAP	CVPR'23	99.86	95.29	66.40	43.00	23.19	100	65.32	58.14	15.28	80.29	9.83	10.13	
MAP \dagger	CVPR'23	<u>99.99</u>	99.86	99.41	96.74	76.20	<u>99.99</u>	100	<u>99.99</u>	97.87	100	97.84	11.36	
MUSE	ICLR'24	99.93	99.64	98.61	94.73	77.56	99.86	<u>99.99</u>	99.83	97.51	100	97.14	35.96	
(c) Dynamic Recovery Method for Missing Modality														
DyMo _c		100	100	99.99	<u>99.71</u>	<u>96.61</u>	100	100	100	99.01	100	98.22	<u>85.31</u>	
DyMo _e		100	100	99.99	<u>99.87</u>	<u>96.81</u>	100	99.98	100	<u>99.22</u>	100	<u>98.43</u>	86.84	

1049

1050

1051 Table S4: Complete results on DVM, CAD, and Infarction under various missing scenarios, compar-
 1052 ing DyMo with incomplete MDL methods, including recovery-based and recovery-free approaches.
 1053 Models marked with \dagger were trained using our proposed incomplete-modality simulation training. In
 1054 addition to the results reported in Tab. 1, we also include results for $\gamma = \{0.1, 0.3, 0.5, 0.9\}$.

Model	DVM Acc (%) \uparrow					CAD AUC (%) \uparrow					Infarction AUC (%) \uparrow				
	Missing Tabular Rate γ					Missing Tabular Rate γ					Missing Tabular Rate γ				
	0	0.1	0.3	0.5	0.7	0.9	1	0	0.1	0.3	0.5	0.7	0.9	1	0
(a) Recovery-based Methods for Missing Modality															
M3Care	98.44	-	-	-	-	-	11.92	85.62	-	-	-	64.99	70.61	-	-
M3Care \dagger	98.94	-	-	-	-	-	93.43	72.48	-	-	-	72.48	83.27	-	-
OnlineMAE	90.92	-	-	-	-	-	89.90	85.22	-	-	-	70.96	84.05	-	-
(b) Recovery-free Methods for Missing Modality															
ModDrop	99.02	98.73	97.68	95.88	93.23	89.80	87.97	85.10	84.56	82.96	80.39	76.65	70.77	69.18	84.76
MTL	<u>99.44</u>	99.43	98.70	97.42	95.53	93.38	92.32	84.87	<u>85.22</u>	<u>83.82</u>	80.98	77.72	73.08	70.23	83.59
MAP	98.86	98.53	97.02	93.83	86.96	74.88	63.15	84.39	83.81	81.52	78.58	75.61	71.39	70.11	84.62
MAP \dagger	99.37	99.10	98.29	96.89	94.83	92.43	91.15	<u>85.26</u>	84.66	82.76	80.14	75.84	70.36	68.76	85.49
MUSE	96.86	-	-	-	-	-	1.64	83.47	-	-	-	53.23	84.40	-	-
(c) Dynamic Recovery Method for Missing Modality															
DyMo _c	99.30	99.10	98.50	<u>97.62</u>	96.31	94.36	93.14	85.14	84.53	82.77	81.16	78.49	<u>73.92</u>	71.02	<u>85.10</u>
DyMo _e	99.50	<u>99.33</u>	98.86	98.08	96.81	94.76	<u>93.36</u>	86.17	85.73	83.84	81.49	<u>78.24</u>	74.01	72.17	83.16

1065

1066

1067

Hager et al., 2023), we employed an early stopping strategy, with a minimal divergence threshold of 0.0001, a maximal number of training epochs (see Tab. S2), and a patience (stopping threshold) of 20 epochs. All models were trained with the same learning rate and batch size as our DyMo (see Tab. S2). We ensured convergence of all methods under this configuration.

C ADDITIONAL EXPERIMENT

C.1 COMPARING AGAINST INCOMPLETE MDL SOTAs (COMPLETE RESULTS)

In Sec. 4.1 of the manuscript, we report results for the most challenging missing scenarios on PolyMNIST, MST, DVM, CAD, and Infarction in Tab. 1, due to space constraints. Here, we provide the complete results in Tab. S3 and Tab. S4.

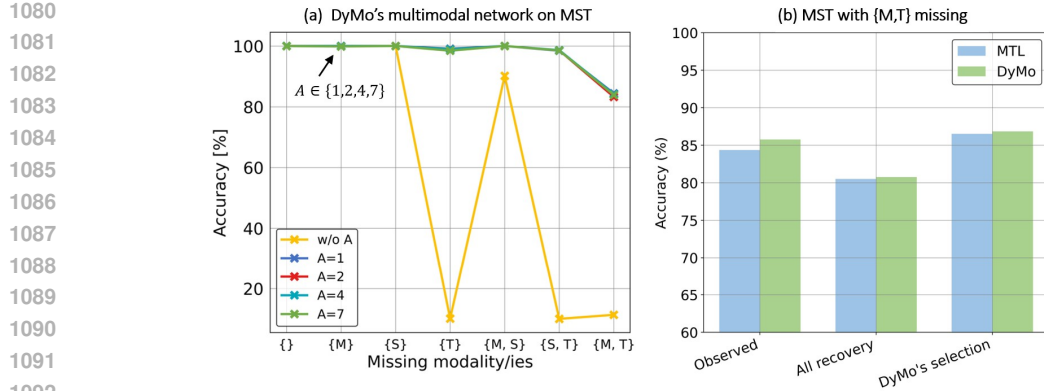


Figure S1: (a) Performance of DyMo_c 's multimodal network on MST under various missing scenarios, evaluated with different numbers of sampled modality subsets (A). $w/o A$ denotes training without our incomplete-modality simulation strategy. (b) Comparison between MTL and DyMo_e on MST with $\{M, T\}$ missing, under different modality inputs: (1) using only non-missing modalities; (2) integrating all recovered modalities without selection; (3) integrating only the recovered modalities selected by DyMo_e .

Table S5: Classification accuracy (%) of DyMo using different modality recovery methods on PolyMNIST under various missing modality rates.

Model	Recovery Method	Publication	Missing Rate η			
			0.2	0.4	0.6	0.8
DyMo_c	MoPoE	ICLR'2021	100	99.99	99.71	96.61
	MMVAE+	ICLR'2023	99.99	99.97	99.79	97.40
	CMVAE	ICLR'2024	100	99.97	99.80	97.69
DyMo_e	MoPoE	ICLR'2021	100	99.99	99.87	96.81
	MMVAE+	ICLR'2023	100	100	99.87	97.39
	CMVAE	ICLR'2024	100	99.99	99.89	97.39

C.2 ABLATION STUDY & GENERALIZABILITY ANALYSIS

Effect of the Incomplete Simulation Training Strategy: We examined the impact of the number of sampled modality subsets (A) during incomplete-modality simulation training on MST under various missing scenarios. As shown in Fig. S1(a), removing our incomplete simulation training leads to a substantial performance drop, *e.g.*, accuracy decreases by 71.91% on MST with missing $\{M, T\}$, compared to models trained with $A = 2$. In contrast, when this training strategy is applied, performance remains stable across different values of A , suggesting that even a small A is sufficient to achieve both efficiency and strong performance.

Efficacy and Applicability of DyMo's Selected Recovered Modalities: We compared DyMo's multimodal network with MTL, a recovery-free transformer-based method, under three input settings: (1) using only non-missing modalities; (2) integrating all recovered modalities without selection; and (3) integrating the recovered modalities selected by DyMo. As shown in Fig. S1(b), for both models, naively integrating all recovered modalities results in lower accuracy than using only the non-missing modalities, indicating that some imputed modalities are task-irrelevant and can negatively affect decision-making. In contrast, integrating only the recovered modalities selected by DyMo improves performance of both models, demonstrating the effectiveness of DyMo's selection algorithm and the applicability of its selected recovered modalities to other models. Moreover, DyMo consistently outperforms MTL across all input settings, which showcases the efficacy of DyMo's network architecture and training strategy.

Generalizability of DyMo Across Different Modality Recovery Methods: To evaluate the robustness and flexibility of DyMo with respect to diverse modality recovery strategies, we conducted experiments using 3 different modality recovery approaches, including **MoPoE** (Sutter et al., 2021), **MMVAE+** (Palumbo et al., 2023), and **CMVAE** (Palumbo et al., 2024), on PolyMNIST under vary-

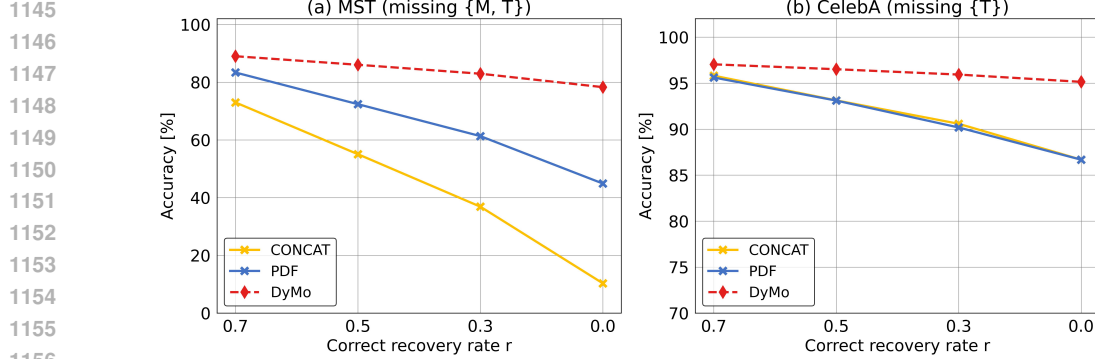
1134

1135 Table S6: Classification accuracy (%) of DyMo using different modality recovery methods on DVM
1136 and Infarction under various missing modality rates.

Model	Recovery Method	DVM $\eta = 0.7$	DVM $\eta = 0.9$	Infarction $\eta = 0.7$	Infarction $\eta = 0.9$
CONCAT	IMI	81.85	67.13	73.75	69.39
DyMo _e	IMI	95.97	94.28	75.96	71.09
CONCAT	TIP	94.74	86.08	75.91	72.04
DyMo _e	TIP	96.81	94.76	76.14	72.96

1143

1144

1157 Figure S2: Results on PolyMNIST (missing {M, T}) and CelebA (missing {T}) with different
1158 correct recovery rates r .
1159

1160

1161

1162 ing missing modality rates. As shown in Tab. S5, DyMo combined with any of these recovery
1163 methods consistently outperforms prior SOTA dynamic/incomplete MDL methods (see Fig. 3 and
1164 Tab. S3). *E.g.*, DyMo_c with CMVAE achieves a 7.6% higher accuracy on PolyMNIST when 80% of
1165 modalities are missing, demonstrating DyMo’s compatibility with multiple modality recovery tech-
1166 niques. In addition, these recovery methods exhibit comparable performance for moderate missing
1167 rates $\eta \in \{0.2, 0.4, 0.6\}$, likely due to their similar reconstruction quality under these conditions.
1168 At a high missing rate ($\eta = 0.8$), DyMo paired with CMVAE achieves the best performance, *e.g.*,
1169 improving MoPoE’s accuracy by 1.08% when both paired with DyMo_c. This outcome is consistent
1170 with the fact that CMVAE, as the latest SOTA recovery network, provides superior reconstruction
1171 quality. Overall, these findings suggest that employing more effective recovery networks can further
1172 enhance DyMo’s performance. Quantitative analyses of reconstruction quality for these recovery
1173 approaches are provided in Appendix C.6.

1174 For DVM and UKBB, we additionally evaluate an alternative recovery method, the iterative multi-
1175 variate imputer (IMI), a widely-used tabular imputation method that recovers missing values using
1176 information from other table columns (Liu et al., 2014). Since IMI relies only on table information
1177 for reconstruction, it performs worse than TIP (Liu et al., 2014). As shown in Tab. S6, with this
1178 weaker reconstructor, CONCAT suffers a large accuracy drop compared to its performance with TIP
1179 (*e.g.*, -18.95% accuracy on DVM with 90% missing tabular features). In contrast, DyMo remains
1180 stable and achieves the best performance under both recovery methods. These results show that
1181 DyMo is not constrained to the reconstruction-quality bottleneck.

1182 To further evaluate DyMo’s robustness to recovery quality, we conducted an extreme simulation
1183 experiment with a controlled correct recovery rate r . For $r \times 100\%$ of the samples, the missing
1184 modalities are imputed with their ground-truth versions; for the remaining $(1 - r) \times 100\%$, the
1185 missing modalities are replaced with zero noise. We evaluate DyMo on MST (missing M, T) and
1186 CelebA (missing T). As shown in Fig. S2, prior static and dynamic fusion methods degrade sharply
1187 as recovery quality deteriorates. In contrast, DyMo remains relatively stable across a wide range of
1188 correct recovery rates, suggesting its ability to effectively disregard unreliable recovered modalities.

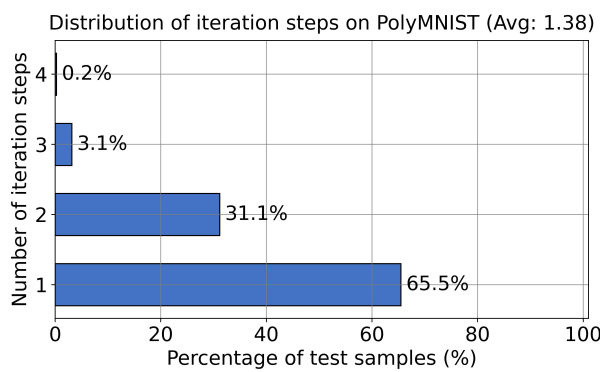


Figure S3: Distribution of iterative selection steps per test sample for DyMo on PolyMNIST with missing modality rate $\eta = 0.8$ (i.e., each sample randomly misses 4 out of 5 modalities). The average number of steps per sample is 1.38.

Table S7: Test loss range on PolyMNIST with 80% missing modalities ($\delta = 0.1$).

Dataset	Dataset Size $ \mathcal{D} $	Min	Max (G in Eq. 2)	$G\sqrt{ \ln 1/\delta / \mathcal{D} }$ in Eq. 2
PolyMNIST	7,000	0.00	4.14	0.0053

C.3 ADAPTIVE INFERENCE ANALYSIS

To study how DyMo dynamically selects task-relevant recovered modalities at inference time, we visualized the distribution of iterative selection steps per sample on PolyMNIST, when 80% of modalities are missing. Fig. S3 shows that samples require different numbers of iterations, reflecting variations in the quality of recovered modalities and the adaptive nature of DyMo. At each iteration, only recovered modalities that provide a non-negligible incremental multimodal task-relevant information are added. In addition, most samples require only 1-2 steps, and the average number of iterations is 1.38, suggesting that although iterative selection introduces some additional computation, the extra cost compared to DyMo w/o iteration selection is moderate.

C.4 TEST TASK LOSS ANALYSIS

We show the test CE loss range for DyMo on PolyMNIST with 60% missing modalities in Tab. S7. The results show that the test CE loss stays within a well-behaved numerical range. The G -related term is extremely small (< 0.006), and thus will not affect the tightness of the lower bound in practice (Eq. 2).

C.5 VISUALIZATION

Latent Feature Space Visualization on Training Data: The MTIR reward of a recovered modality in DyMo is based on the representation shift in the latent space relative to the training distribution after adding that modality. We used t-SNE to visualize the multimodal latent space learnt by DyMo’s multimodal network on training data under various missing scenarios. As shown in Fig. S4, samples from different classes are generally well-separated, demonstrating that DyMo effectively learns a structured feature space suitable for reward calculation.

Input-Level Case Study: To understand which recovered modalities are selected by DyMo, we conduct input-level case studies comparing DyMo with other dynamic/static fusion methods, as shown in Fig. 5(b) in the manuscript and Fig S5. The results indicate that (1) the recovery method may generate modalities of varying qualities across samples; (2) existing dynamic MDL methods that rely solely on modality-specific information for estimating modality importance often fail to

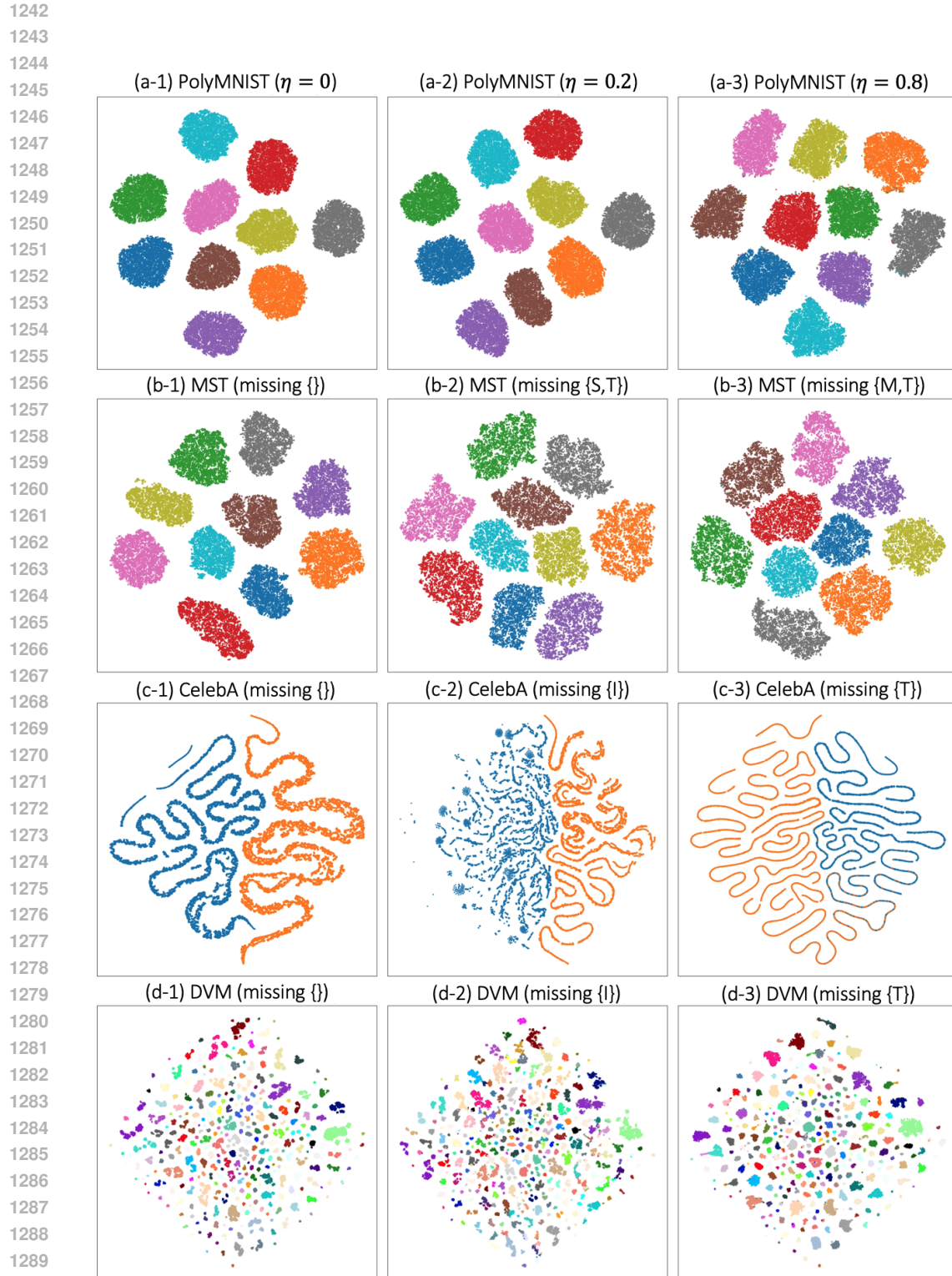


Figure S4: t-SNE visualization of DyMo_c 's multimodal network on the training data of (a) PolyMNIST, (b) MST, (c) CelebA, and (d) DVM under various missing scenarios. Colors denote different class labels.

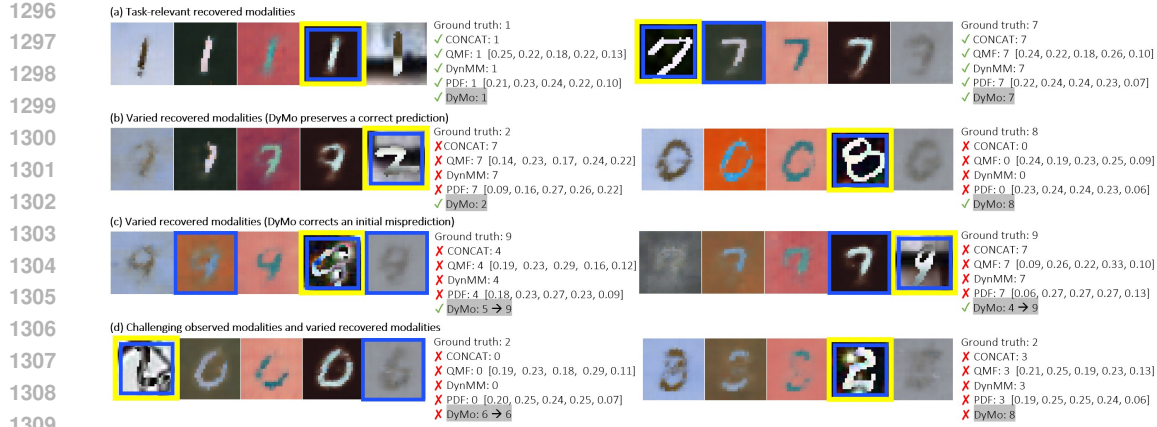


Figure S5: Extending the cases shown in Fig. 5(b), this figure presents additional representative examples of model predictions on PolyMNIST with missing rate $\eta = 0.8$ for DyMo and static/dynamic multimodal fusion methods. The sub-figures illustrate: (a) all recovered modalities are task-relevant; (b) recovered modalities vary in quality, and DyMo preserves correct predictions by disregarding unreliable recoveries; (c) recovered modalities vary in quality, and DyMo corrects initial mispredictions by incorporating task-relevant recovered modalities; (d) particularly challenging cases with limited task-relevant information in both non-missing and recovered modalities. Yellow boxes indicate non-missing modalities, and blue boxes indicate modalities selected by DyMo_c. ✓ denotes correct predictions, while ✗ denotes incorrect predictions. For QMF and PDF, which perform dynamic weighted fusion, we report the weights assigned to each modality for every sample.

identify semantically misaligned recovery (*e.g.*, right case in Fig. S5(b)), which can degrade model performance; and (3) DyMo, however, alleviates this limitation by selectively incorporating beneficial recovery while disregarding unreliable one, thereby improving overall performance. Moreover, Fig. S5(d) illustrates particularly challenging cases for all models, where both non-missing and recovered modalities provide limited task-relevant information. In these rare and difficult cases, DyMo may not fully correct its initial mispredictions, suggesting that the use of more advanced recovery methods could further enhance performance.

C.6 RECOVERED MODALITY ANALYSIS

VAE-based Reconstruction Analysis: Fig. 5(b) in the manuscript and Appendix C.5 present examples of recovered modalities. We further provide a quantitative analysis of these reconstructions. Specifically, We evaluated the reconstruction performance of VAE-based modality recovery methods (*i.e.*, MoPoE, MMVAE+, and CMVAE) on PolyMNIST. Following prior studies (Palumbo et al., 2023; Sutter et al., 2021), we assessed cross-modal generation using two complementary metrics: (i) semantic generative coherence, measured by the accuracy of generated modalities (*i.e.*, conditional coherence accuracy); and (ii) generative quality, measured by the similarity between generated and real samples using the Fréchet Inception Distance (FID) score (Heusel et al., 2017). Additional details of these metrics can be found in Appendix D.3 of (Palumbo et al., 2023). As shown in Fig. S6, CMVAE consistently outperforms the other methods in both cohenrence and quality across different numbers of input modalities. This finding aligns with the observation that DyMo combined with CMVAE achieves the best classification performance (see Tab. S5). Notably, while MoPoE performs substantially worse than MMVAE+ and CMVAE, DyMo exhibits smaller performance gaps across all three recovery methods. This demonstrates that DyMo is robust to different recovery techniques by dynamically integrating task-relevant recovered modalities while disregarding unreliable ones, highlighting its selective and adaptive behavior.

Table Reconstruction Analysis: Tab. S8 and Fig. S7 report the reconstruction results of tabular features for DVM and UKBB under full-table missingness, respectively. Categorical features are evaluated using accuracy, while continuous features are assessed with mean squared error (MSE). The results show that most tabular features are accurately reconstructed, *e.g.*, *color* in DVM (Acc: 82.46%), suggesting that their integration can benefit the target classification task. Some tabular

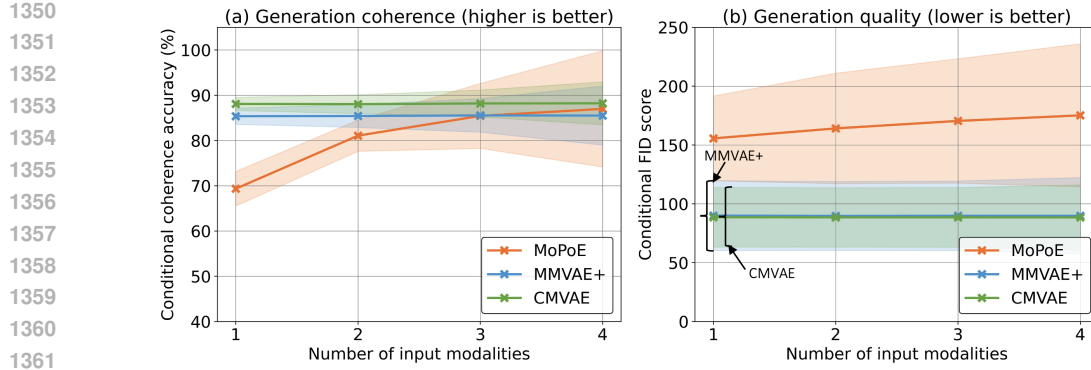


Figure S6: Reconstruction performance of different VAE-based recovery methods on PolyMNIST: (a) reconstruction coherence (higher is better), (b) reconstruction quality measured by FID (lower is better).

Table S8: Reconstruction performance of 17 tabular features (4 categorical and 13 continuous) using TIP on DVM under full-table missingness (*i.e.*, $\gamma = 1$). **Cat** denotes whether a tabular feature is categorical, and N_{unq} represents the number of unique values for each categorical feature.

Tabular Feature	Cat	N_{unq}	MSE ↓	Acc (%) ↑	Tabular Feature	Cat	N_{unq}	MSE ↓	Acc (%) ↑
Advertisement month (Adv_month)	✗	-	1.2340	-	Height	✗	-	0.3234	-
Advertisement year (Adv_year)	✗	-	0.4448	-	Length	✗	-	0.4272	-
Bodytype	✓	13	-	82.25	Price	✗	-	0.2921	-
Color	✓	22	-	82.46	Registration year (Reg_year)	✗	-	0.2622	-
Number of doors (Door_num)	✗	-	0.3641	-	Miles runned (Runned_Miles)	✗	-	0.6962	-
Engine size (Engine_size)	✗	-	0.3818	-	Number of seats (Seat_num)	✗	-	0.4601	-
Entry prize (Entry_prize)	✗	-	0.2908	-	Wheelbase	✗	-	0.5938	-
Fuel type (Fuel_type)	✓	12	-	64.45	Width	✗	-	0.5873	-
Gearbox	✓	3	-	73.24					

features, however, exhibit low reconstruction performance, likely due to their relatively weak correlations with the image modality. Examples include *fuel type* in DVM (Acc: 64.45%) and *smoking status* in UKBB (Acc: 4.4%). In real-world applications, though, tabular features are more often partially missing rather than entirely absent (Wu et al., 2024b; Xue et al., 2024). Under a tabular missing rate $\gamma = 0.5$, we observed that the reconstruction performance of these challenging features improves substantially, *e.g.*, *fuel type* in DVM (64.45% \rightarrow 87.13%) and *smoking status* in UKBB (4.4% \rightarrow 86.99%). These findings suggest that the proposed DyMo can generalize well to practical scenarios, where partial missingness is more common than full-table missingness.

D DISCUSSION

Beyond Classification Tasks: While this paper primarily focuses on classification tasks, the DyMo’s framework can be extended to a broader range of multimodal tasks. The key adaptation is to replace the cross-entropy (CE) term with the appropriate likelihood-based loss for the target task. Many multimodal tasks, *e.g.*, detection, segmentation, and sequence-to-sequence modelling, can be trained using probabilistic losses, and thus the same mutual information decomposition, $I(Y; Z) = H(Y) - H(Y|Z)$, remains applicable. In specific: (1) segmentation: MTIR can operate on the averaged per-pixel CE loss; (2) detection: MTIR can incorporate both classification and localization likelihoods as the task loss; and (3) sequence-to-sequence modelling: MTIR can aggregate token-level CE losses to guide modality selection.

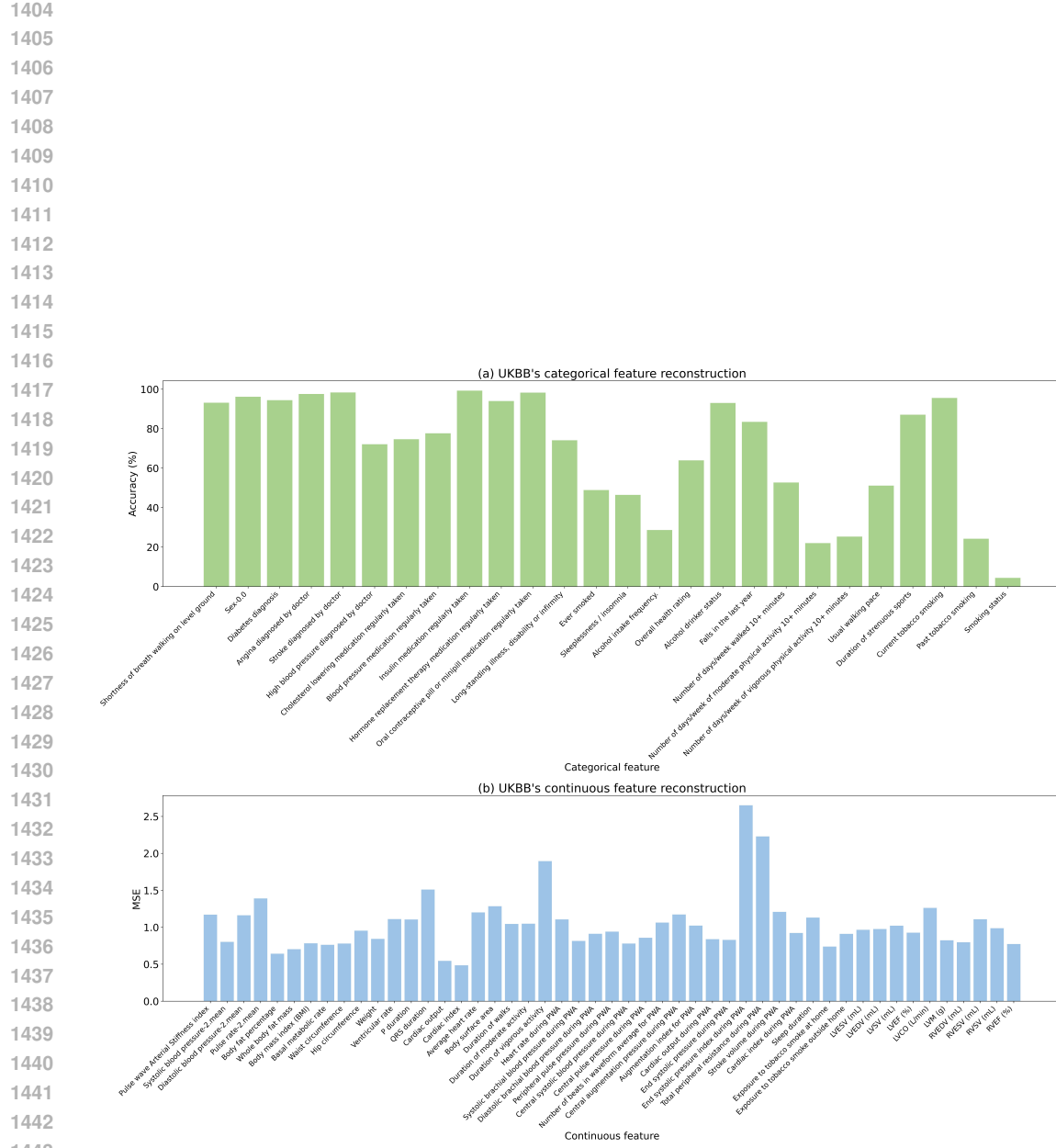


Figure S7: Reconstruction performance of 75 tabular features (26 categorical and 49 continuous) using TIP on UKBB under full-table missingness (i.e., $\gamma = 1$).